nature structural & molecular biology

Article

https://doi.org/10.1038/s41594-025-01726-y

Translational activators align mRNAs at the small mitoribosomal subunit for translation initiation

Received: 1 January 2025

Accepted: 28 October 2025

Published online: 03 December 2025

Check for updates

Joseph B. Bridgers[1,6], Andreas Carlström[2,3,6], Dawafuti Sherpa[4,6], Mary T. Couvillion[1], Urška Rovšnik[3], Jingjing Gao[4], Bowen Wan[1], Sichen Shao[4,5] ✉, Martin Ott[2,3] ✉ & L. Stirling Churchman[1] ✉

Mitochondrial gene expression is essential for oxidative phosphorylation. Mitochondrial-encoded mRNAs are translated by dedicated mitochondrial ribosomes (mitoribosomes), whose regulation remains elusive. In *Saccharomyces cerevisiae*, nuclear-encoded mitochondrial translational activators (TAs) facilitate transcript-specific translation by a yet unknown mechanism. Here, we investigated the function of TAs containing RNA-binding pentatricopeptide repeats using selective mitoribosome profiling and cryo-electron microscopy (cryo-EM) structural analysis. These analyses show that TAs exhibit strong selectivity for mitoribosomes initiating on their target transcripts. Moreover, TA–mitoribosome footprints indicate that TAs recruit mitoribosomes proximal to the start codon. Two cryo-EM structures of mRNA–TA complexes bound to mitoribosomes stalled in the post-initiation, pre-elongation state revealed the general mechanism of TA action. Specifically, the TAs bind to structural elements in the 5′ untranslated region of the client mRNA and the mRNA channel exit to align the mRNA in the small subunit during initiation. Our findings provide a mechanistic basis for understanding how mitochondria achieve transcript-specific translation initiation without relying on general sequence elements to position mitoribosomes at start codons.

Mitochondria derive from an alphaproteobacteria ancestor and have retained a reduced genome, which encodes critical components of the oxidative phosphorylation (OXPHOS) complexes. The mitochondrial genome of *Saccharomyces cerevisiae* (budding yeast) encodes seven OXPHOS proteins and one component of the mitochondrial ribosome (mitoribosome). These genes are transcribed by a dedicated mitochondrial RNA polymerase and translated by specialized mitoribosomes[1]. The remaining 38 OXPHOS subunits are transcribed from the nuclear genome and are synthesized on cytoplasmic ribosomes before their import into mitochondria. Translation of nuclear and mitochondrial subunits belonging to the same OXPHOS complex is coordinated to prevent the production of excess, unassembled subunits that can be detrimental to the cell through the generation of reactive oxygen species and chronic proteostatic stress[2–6].

Despite sharing some similarities with their bacterial ancestors, mitoribosomes have diverged greatly from bacterial ribosomes,

[1]Department of Genetics, Blavatnik Institute, Harvard Medical School, Boston, MA, USA. [2]Department of Biochemistry and Biophysics, Stockholm University, Stockholm, Sweden. [3]Department of Medical Biochemistry and Cell Biology, Institute of Biomedicine, University of Gothenburg, Gothenburg, Sweden. [4]Department of Cell Biology, Harvard Medical School, Boston, MA, USA. [5]Howard Hughes Medical Institute, Chevy Chase, MD, USA. [6]These authors contributed equally: Joseph B. Bridgers, Andreas Carlström, Dawafuti Sherpa. ✉e-mail: sichen_shao@hms.harvard.edu; martin.ott@gu.se; churchman@genetics.med.harvard.edu

as evidenced by substantially differing structures and mechanisms of translation[7–11]. Bacterial translation initiation often uses the Shine–Dalgarno (SD) sequence motif, which is found in the 5′ untranslated region (5′ UTR) of mRNAs just upstream of the start codon. The SD motif base pairs with the anti-SD sequence in the 16S rRNA, which helps to recruit the mRNA to the small subunit (SSU). The distance between the SD sequence and the start codon is important to align the start codon with the ribosomal peptidyl-tRNA-binding site (P-site) to ensure fidelity and efficiency of translation initiation[12]. How translation of mitochondrial mRNAs is initiated is yet unknown because mRNAs in mitochondria lack SD-like motifs and the mitoribosome lacks an anti-SD sequence.

Early genetic work in yeast identified a group of nuclear-encoded mitochondrial proteins that are necessary for translation of individual mitochondrial transcripts and were termed translational activators (TAs)[6,13]. TAs have been proposed to recruit their target mRNAs to the mitoribosome and aid in translation initiation[6,13,14]. A subset of TAs also participate in translation feedback loops to control synthesis of specific proteins in relation to the efficiency by which they can assemble into OXPHOS complexes[15–18]. TA binding to mRNAs is supported by specific helical structural motifs, including pentatricopeptide repeats (PPRs), which have been proposed to mediate sequence-specific mRNA binding[19–25]. Several studies revealed functional genetic interactions between the TAs and the 5′ UTRs of their target transcripts but only a few of the PPR-containing TAs have been shown to directly bind RNA[26–29]. Moreover, genetic and protein proximity mapping revealed that TAs bind to the mRNA channel exit (MCE) of the SSU[14,30], which would be in line with a role in translation initiation. While it is clear that TAs are required for the translation of specific transcripts within mitochondria, how TAs engage with the 5′ UTR or the mitoribosome to support translation initiation and elongation remains unresolved.

In this study, we determined when and how TAs engage with the mitoribosome during translation. By establishing selective ribosome profiling for mitoribosomes (sel-mitoRP), we determined when TAs bind the mitoribosome on target transcripts. These analyses revealed that TAs are highly enriched on mitoribosomes near the translation initiation site of their client mRNA and that they are released soon after the onset of elongation, confirming a role in initiation. Moreover, TA binding patterns in the 5′ UTR suggest the stabilization of specific mRNA folds by complex formation between this portion of the mRNA and the TAs. Consequently, inhibiting translation elongation by genetic ablation of a general elongation factor led to the accumulation of post-initiation, pre-elongation mitoribosomes with bound TAs. Structure determination using single-particle cryo-electron microscopy (cryo-EM) resolved two distinct TA–mitoribosome complexes with bound mRNA. The structures revealed how the *ATP8* and the *ATP9* TAs bind to the mitoribosome, with the 5′ UTR of their client mRNA wrapped around the TA(s). Additional structural analyses of *ATP9* TA complexes affinity-purified with elongation-competent mitoribosomes further corroborated the role of TAs specifically in translation initiation. Together, our data demonstrate that TAs function to recruit their target transcript to the mitoribosome and act as molecular guides to position the transcript in the mRNA channel for proper translation initiation.

Interaction of TAs with the mitochondrial translatome

The RNA-binding capabilities of PPR proteins and their localization to the MCE position them as candidate factors for serving an SD-like function in recruiting their target transcript to the mitoribosome. To investigate the molecular functions of TAs containing PPR motifs during mitochondrial translation, we adapted sel-mitoRP (Fig. 1a,b and Extended Data Fig. 1)[31,32]. This method determines when specific factors interact with the mitoribosome at codon resolution. Specifically, lysate from crosslinked cells was treated with RNAse and total ribosomes were isolated. Mitoribosome subpopulations bound by a TA of interest were purified by affinity chromatography and the ribosome-protected RNA fragments were analyzed by sequencing (Fig. 1b). We first performed sel-mitoRP for Pet111, the TA of *COX2* (ref. 33), and for mitochondrial ribosomal protein of the SSU 17 (Mrps17), a constitutive subunit of the mitoribosome. We previously showed that mitoribosome footprint density on the *COX2* transcript is lost upon deletion of *PET111* (ref. 2). Consequently, sel-mitoRP analyses demonstrated a strong and specific enrichment of Pet111–mitoribosome footprints on *COX2*, with the highest enrichment of RNA footprints in the 5′ UTR, approximately 200 times that of the total mitoribosome control (Fig. 1c,d and Extended Data Fig. 2a). The enrichment of Pet111–mitoribosome footprints just upstream of the start codon aligns with previous studies that showed the importance of the *COX2* 5′ UTR in Pet111 translational activation[28,34].

To determine whether the other mitochondrial TAs are as specific as Pet111, we performed sel-mitoRP for TAs containing PPR motifs: Pet309 (TA for *COX1*), Aep3 (TA for *ATP8*), Atp22 (TA for *ATP6*), Cbp1 (TA for *COB*) and Aep1 and Aep2 (TAs for *ATP9*) (Fig. 1c,d and Extended Data Figs. 1 and 2a)[20–25]. Similar to Pet111, the majority of the TAs showed a strong enrichment on mitoribosomes translating their target transcript (Fig. 1c). The only exception to this trend was Cbp1, which did not show a specific enrichment on the *COB* transcript, which may be explained by its role as part of a translational feedback loop[18].

TA–mitoribosome footprints are enriched upstream of start codons

Closer examination of the target transcript for each TA indicated a strong enrichment of TA–mitoribosome footprints in the 5′ UTR, decreasing abruptly after the start codon and tailing off further after early elongation (Fig. 1d). This enrichment at the 5′ end of open reading frames and depletion from the 3′ end argue that the TAs leave the ribosome soon after initiation. To gain more insights into how TAs influence initiation, we performed a closer analysis of the footprints around translation start sites. These footprints represent those selected for during library preparation to be between 35 and 45 nt in length, a typical window for ribosome profiling experiments. Nevertheless, the locations and heterogeneity of footprint ends shed light on the state of the ribosome[35–37].

We began with footprints of *ATP9* mRNA, which are highly abundant (Fig. 1c) because of the high rates of Atp9 synthesis required to support assembly of the ATP synthase rotor that contains ten Atp9 subunits. Comparing footprints from Mrps17 sel-mitoRP with and without formaldehyde crosslinking revealed different footprints for the initiating mitoribosome. The initiating mitoribosome on *ATP9* in noncrosslinked mitoribosome profiling yielded a footprint with 5′ ends 16 nt upstream of the start codon and 3′ ends approximately 22 nt downstream of the start codon (Fig. 2a), in line with the expected size and position of a mitoribosome-protected fragment with the start codon positioned in the P-site[2]. Interestingly, crosslinking stabilized a larger footprint in the 5′ UTR with 5′ ends approximately 38 nt upstream of the start codon and variable 3′ ends within a few nucleotides of the start codon (Fig. 2a). This upstream footprint was also highly enriched in sel-mitoRP for the *ATP9* TAs, Aep1 and Aep2 (Fig. 2a). Because of an empty aminoacyl site (A-site) of the initiating ribosome, cytosolic ribosomes can have a truncated 3′ footprint end near the start codon following RNase I cleavage inside the ribosome[35–37]. Therefore, we hypothesized that the larger upstream footprint might reflect an initiating TA–mitoribosome complex with the TAs extending the 5′ end of the mitoribosome footprint through increased protection of the mRNA. Additionally, the 3′ end of the footprint is truncated from the expected +22 position, likely because of RNase I cutting within the initiating mitoribosome. Full-length TA–mitoribosome footprints starting at −38 and ending at +22 (60 nt) would be beyond the size range selected. Likewise, without crosslinking to stabilize the TAs,

https://doi.org/10.1038/s41594-025-01726-y

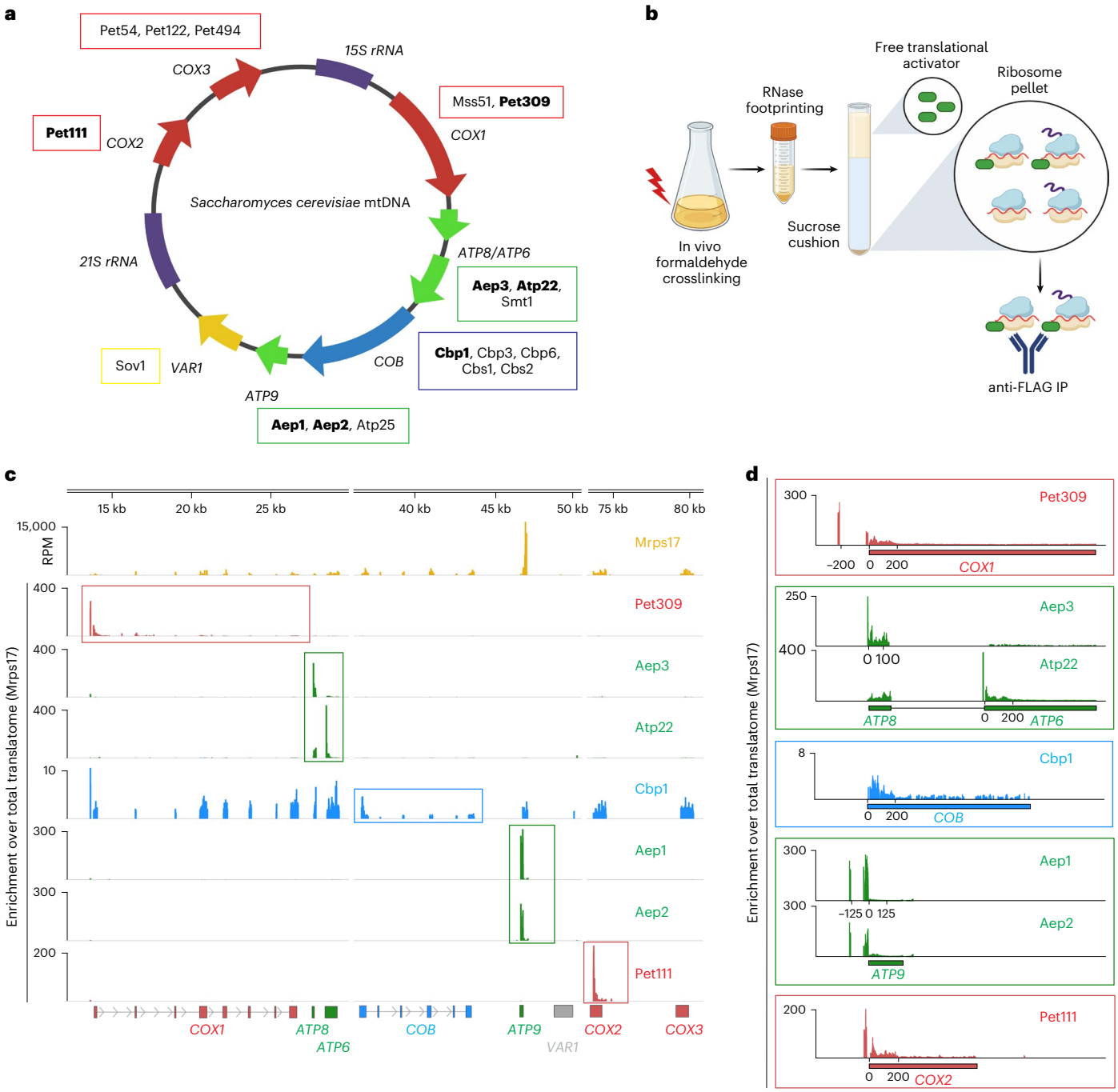

Fig. 1 | PPR domain TAs are selectively enriched at translation initiation. **a**, Schematic of *S. cerevisiae* mitochondrial genome. The locations of the 15S and 21S rRNAs are labeled in purple and the protein-coding genes are color-coded according to the complex they belong to: ATP synthase in green, complex III in blue and complex IV in red. Translational regulators are boxed in the corresponding color next to their target transcript. Proteins analyzed in **c** are highlighted in bold. **b**, Overview of selective mitoribosome profiling (sel-mitoRP). **c**, Top: inferred A-site counts for a total mitoribosome control dataset (Mrps17). Bottom: sel-mitoRP of the indicated TA normalized to the total mitoribosome control (Mrps17). The boxed genes are the known translation target of the given TA. **d**, Zoomed-in view of enrichment for the given TA on the boxed target gene from **c**. The *x* axis is labeled with nucleotide distances relative to the start codon. All data consist of combined reads from at least two biological replicates. Panels **a** and **b** created with BioRender.com. RPM, reads per million mapped reads.

footprints because of RNase I internal cleavage would be too small to be sequenced, which is likely why they were not observed in the natively prepared library.

We next analyzed the 5′ and 3′ ends of the footprints from sel-mitoRP for the other PPR proteins to determine whether they had patterns similar to Aep1 and Aep2 in the 5′ UTR of their target transcripts (Fig. 2b–d and Extended Data Fig. 2b–g). Sel-mitoRP data for Atp22 and Pet309, the TAs for *ATP6* and *COX1*, respectively, exhibited footprint ends with similar patterns to those for Aep1 and Aep2 (Fig. 2b,c). Aep3 mitoribosomes yielded a 3′-shifted RNA footprint with the 5′ end of the footprint positioned approximately 30 nt upstream of the start codon and a variable 3′ end positioned a few nucleotides downstream of the start codon (Fig. 2b). We surmise that this footprint reflects a similar TA–mitoribosome complex to those observed for the complexes described above, with the P-site positioned over the start codon. However, as Aep3 is a smaller protein, it likely protects less

https://doi.org/10.1038/s41594-025-01726-y

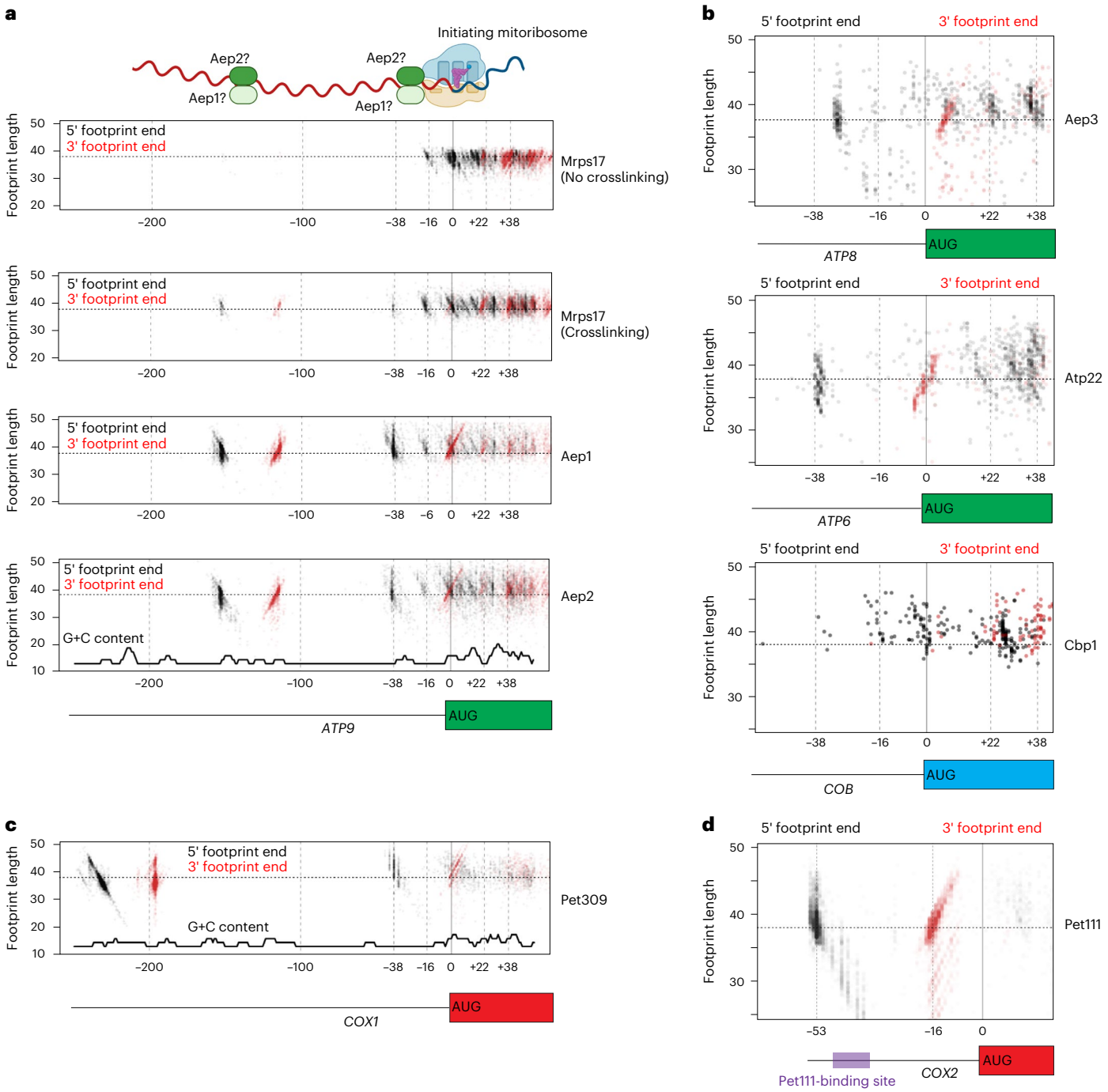

Fig. 2 | Visualizing TA–mitoribosome footprints in the 5′ UTR. a, The 5′ and 3′ ends of footprints from total mitoribosome profiling (Mrps17) either with or without formaldehyde crosslinking were plotted in relation to the start codon of *ATP9* and compared to the footprints from Aep1 and Aep2 sel-mitoRP. The horizontal dashed line indicates a fragment length of 38 nt, which is the approximate size of a mitoribosome footprint at initiation. G+C content of the *ATP9* transcript is plotted along the bottom of the Aep2 footprint data with a scale from 0–1 (not shown). Top: diagram depicting the position of an initiating mitoribosome footprint with its 5′ end at −16 and its 3′ end at +22. Aep1 and Aep2 are depicted upstream of the initiating mitoribosome to indicate the potential binding sites of Aep1 or Aep2 in the 5′ UTR and the subsequent extension of the 5′ end from −16 to −38. **b**, The 5′ and 3′ footprint ends for each sel-mitoRP dataset with footprints that abut the start codon, indicating a potential TA–mitoribosome complex at initiation. **c**, The 5′ and 3′ footprint ends from Pet309 sel-mitoRP plotted around the start codon of *COX1*. Bottom: G+C content of the transcript is plotted as a solid black line with a scale from 0–1 (not shown). **d**, The 5′ and 3′ footprint ends from Pet111 sel-mitoRP plotted around the start codon of *COX2*. The known Pet111-binding site in the 5′ UTR of *COX2* is boxed in purple. All data consist of combined reads from at least two biological replicates. Panel **a** created with BioRender.com.

upstream RNA and the fragments resulting from cleavage over the start codon (~30 nt) are too small to be detected, resulting in an apparent shift in the 3′ ends. Presumably, we would observe smaller Aep3–mitoribosome footprints with 3′ ends positioned at the start codon if smaller footprints were captured. Lastly, the Cbp1 footprint in the *COB* UTR was less intense compared to the downstream initiating footprint, perhaps because of its reduced enrichment on its target transcript.

The Pet111 sel-mitoRP footprints had a unique pattern in the 5′ UTR with well-defined 5′ ends positioned 53 nt upstream of the start codon and more variable 3′ ends positioned around 16 nt upstream of the start

https://doi.org/10.1038/s41594-025-01726-y

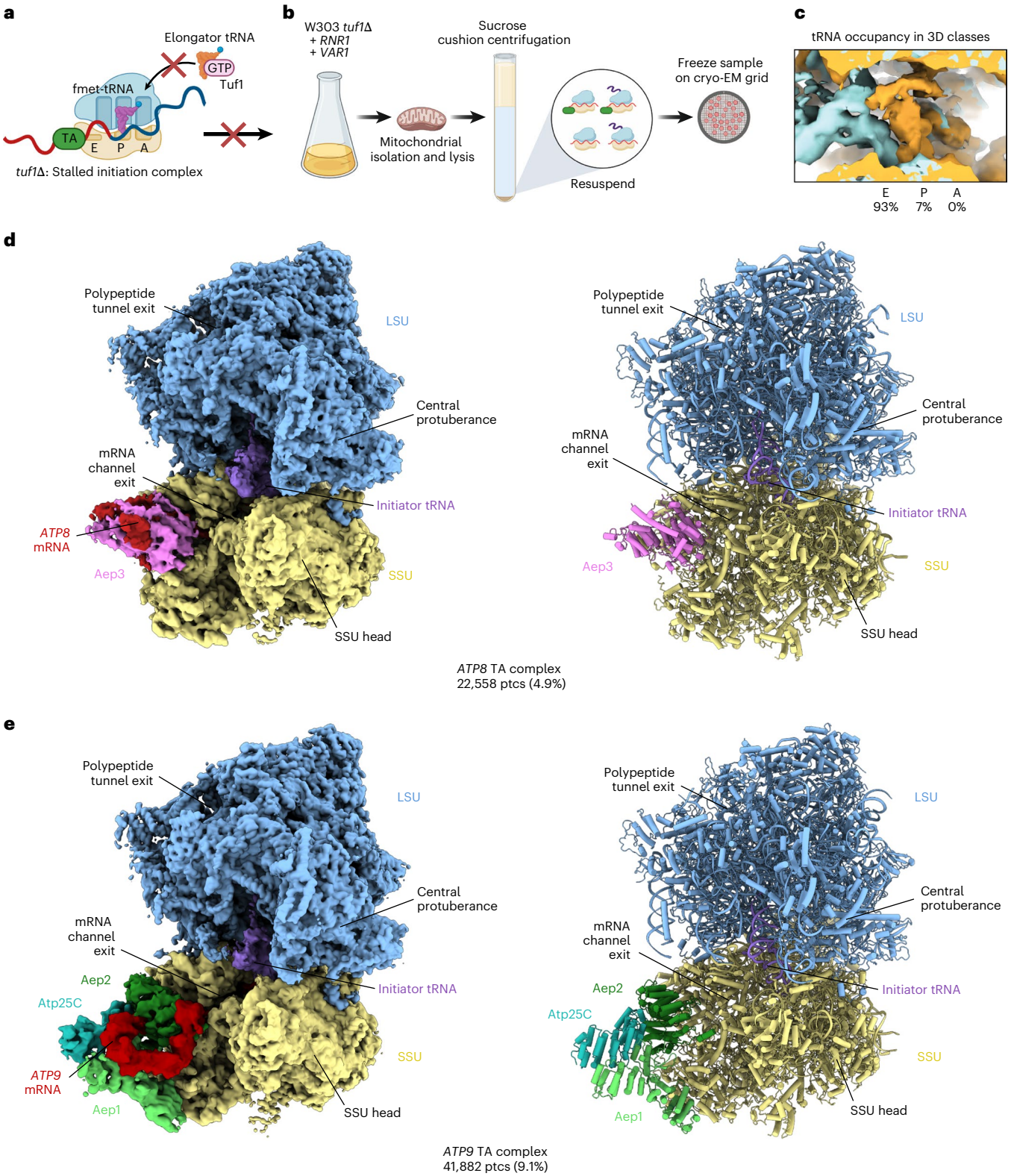

Fig. 3 | *ATP8* and *ATP9* TAs bind mitoribosomes stalled in a post-initiation, pre-elongation state. a, Schematic of *TUF1* deletion, which leads to stalling of mitoribosomes at initiation by preventing the recruitment of elongator tRNAs. **b**, Overview of sample preparation of *tuf1Δ* strain mitoribosomes for cryo-EM analysis. **c**, Occupancy of tRNA densities in the tRNA-binding sites on the mtSSU obtained after focused 3D classification on 461,825 monosome particles. In total, 93% of classes showed tRNA density in the E-site and 7% showed tRNA density in the P-site. No density could be visualized in the A-site in any of the classes, which is indicative of ribosomes able to initiate translation but not proceed to elongation. **d**, Cryo-EM density map (left) and structural model (right) of the *ATP8* mRNA (red) and its TA, Aep3 (lavender), bound to the MCE on the SSU of the mitoribosome. **e**, Cryo-EM density map (left) and structural model (right) of the *ATP9* mRNA (red) and a complex of its TAs Aep1 (light green), Aep2 (forest green) and Atp25C (cyan) bound to the MCE on the SSU of the mitoribosome. Both cryo-EM density maps in **d**,**e** are displayed as composite density maps of their respective consensus refinement and locally refined maps (LSU, SSU body, SSU head and TA; Extended Data Fig. 5d). Panels **a** and **c** created with BioRender.com. ptcs, particles.

https://doi.org/10.1038/s41594-025-01726-y

Table 1 | Cryo-EM data collection, refinement and validation statistics

	Aep1–Aep2–Atp25–mitoribosome (EMD-52281, EMD-52235, EMD-52270, EMD-52252, EMD-52256, EMD-52257) (PDB 9HLZ)	Aep3–mitoribosome (EMD-52283, EMD-52277, EMD-52276, EMD-52278, EMD-52279, EMD-52280) (PDB 9HM0)
Data collection and processing		
Magnification	165,000	165,000
Voltage (kV)	300	300
Electron exposure (e^- per Å^2)	38	38
Defocus range (μm)	−0.4 to −2.6	−0.4 to −2.6
Pixel size (Å)	0.828	0.828
Symmetry imposed	C_1	C_1
Initial particle images (no.)	4,643,077	4,643,077
Final particle images (no.)	41,190	22,558
Map resolution (Å) (consensus/LSU/SSU body/SSU head/TA complex)	3.0/2.9/2.9/2.9/3.8	3.0/2.8/3.0/3.0/3.7
FSC threshold	0.143	0.143
Map resolution range (Å)	2.6–8	2.5–8
Refinement		
Initial model used (PDB code)	5MRC, 8OM4, AlphaFold3	5MRC, 8OM4, AlphaFold3
Model resolution (Å)	3.4	3.3
FSC threshold	0.5	0.5
Map sharpening *B* factor (Å^2) (consensus/LSU/SSU body/SSU head/TA complex)	−41/−47/−36/−40/−50	−25/−30/−25/−30/−30
Model composition		
Nonhydrogen atoms	218,112	213,189
Protein residues	15,702	15,088
Ligands	Mg^{2+}: 299	Mg^{2+}: 317
	GTP: 1	GTP: 1
B factors (Å^2)		
Protein	84.9	78.1
Ligand	35.0	33.1
R.m.s. deviations		
Bond lengths (Å)	0.004	0.005
Bond angles (°)	0.779	0.830
Validation		
MolProbity score	1.71	1.72
Clashscore	7.63	7.64
Poor rotamers (%)	0.00	0.01
Ramachandran plot		
Favored (%)	95.74	95.64
Allowed (%)	4.26	4.36
Disallowed (%)	0.00	0.00

codon (Fig. 2d and Extended Data Fig. 2f). This correlates well with the experimentally defined Pet111-binding site in the 5′ UTR of *COX2* (ref. 28) and an AlphaFold3 (ref. 38) model of Pet111 bound to the *COX2* 5′ UTR (Extended Data Fig. 3a–d). All these TA–mitoribosome footprints suggest that they could function similarly to Aep1 and Aep2 by binding to the mitoribosome and upstream RNA to position the mitoribosome at the start codon.

In addition to the TA–mitoribosome footprints proximal to the start codon, Aep1, Aep2 and Pet309 sel-mitoRP revealed RNase-protected fragments further upstream in the 5′ UTR (Fig. 2a,c). Specifically, a second set of mitoribosome footprints for Aep1 and Aep2 sel-mitoRP was found over 100 nt upstream of the *ATP9* start codon and Pet309 sel-mitoRP upstream footprints were more than 200 nt upstream of the *COX1* start codon (Fig. 2a,c). These footprints could represent a separate population of mitoribosomes or they could be RNA fragments interacting with the initiating mitoribosome through looping and folding of the 5′ UTR. Although the patterning and positioning of the RNA footprints differed across the TAs studied, in all cases, the TAs engaged with the mitoribosome proximal to the start codon of their target transcript and were disenriched during early elongation, suggesting a role in RNA recruitment to the mitoribosome during translation initiation.

https://doi.org/10.1038/s41594-025-01726-y

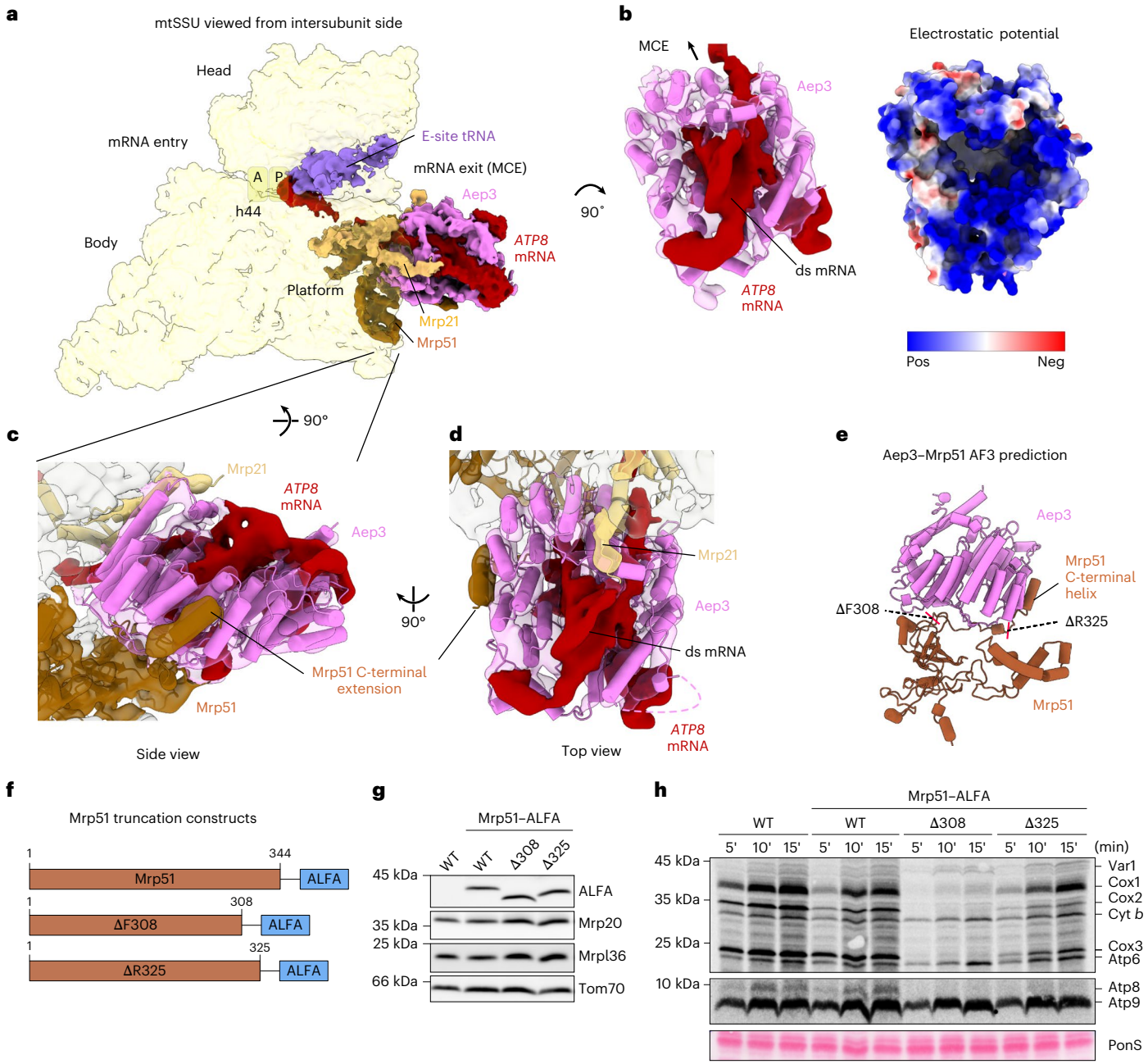

Fig. 4 | Structure of Aep3 bound to the initiating mitoribosome and 5′ UTR of *ATP8* mRNA. a, Top view of the mtSSU (yellow), viewed from the intersubunit side, demonstrating the interaction of the TA Aep3 (lavender) with *ATP8* mRNA (red) and mitoribosomal proteins Mrp51 and Mrp21 at the MCE. Density for the initiator tRNA (purple) is present in the E-site. **b**, Left: structural model of Aep3 (lavender) in a locally filtered map displaying the TA density together with the *ATP8* mRNA density (red). A double-stranded segment of mRNA (ds mRNA) is located in a positively charged binding pocket made up from the PPR motifs of Aep3. Right: surface map representation of Aep3 colored according to electrostatic potential with positively charged residues in blue and negatively charged residues in red. **c**,**d**, Side view (**c**) and top view (**d**) of Aep3 interacting with the SSU proteins Mrp51 (brown) and Mrp21 (light brown) at the MCE, where an extended C-terminal density of Mrp51 forms a binding platform. The dashed line represents residues 33–52, which were not modeled in the Aep3 structure. **e**, AlphaFold3 prediction of Aep3 in complex with Mrp51, demonstrating the C-terminal helix of Mrp51 predicted to interact with PPR helices of Aep3. Dashed lines indicate the chosen sites for Mrp51 C-terminal truncations (ΔF308 and ΔR325). **f**, Schematic showing the Mrp51 truncation constructs, generated by addition of a C-terminal ALFA epitope tag through homologous recombination at indicated residues. **g**, Steady-state levels of proteins extracted from cells containing the different Mrp51–ALFA constructs. The maintained level of the mitoribosomal protein Mrp20 indicates intact mtDNA. Tom70 was used as a loading control. Two biological replicates were performed and yielded similar results. **h**, In vivo radiolabeling using [^{35}S]methionine to monitor mitochondrial translation in cells with wild-type Mrp51 (WT), Mrp51–ALFA or Mrp51–ALFA with C-terminal truncations (Δ308 and Δ325). Samples were taken after 5, 10 and 15 min, TCA-precipitated and analyzed using SDS–PAGE with an 18% gel followed by autoradiography. Three biological replicates were performed with similar results. Cryo-EM densities in **b**–**d** are visualized with maps filtered according to their local resolution, with density thresholds (σ) set to 0.06 for both proteins and mRNA. neg, negative; pos, positive.

Cryo-EM structures of initiating mitoribosomes

Sel-mitoRP revealed that TAs bind to mitoribosomes transiently during early stages of translation through the formation of specific contacts with the mitoribosomes and their client mRNA. Inspired by these results and to gain a more detailed perspective, we aimed to stall mitoribosomes at initiation to determine their structures by single-particle cryo-EM (Extended Data Fig. 4). We genetically induced initiation-stalled mitoribosomes by deleting *TUF1*, encoding the homolog of the bacterial translation elongation factor EF-Tu. Without Tuf1, elongator tRNAs cannot be delivered to the A-site; hence, mitoribosomes are trapped in a post-initiation, pre-elongation state with an initiator fMet-tRNA in the P-site or E-site[39] (Fig. 3a). The *TUF1* deletion was generated in a background overexpressing *RNR1* and *VAR1*, an established strategy to preserve mitochondrial DNA (mtDNA) integrity in the face of defective mitochondrial translation[40] (Extended Data Fig. 5a,b). Impaired mitochondrial translation following deletion of *TUF1* was evidenced by the lack of growth on respiratory medium and abolished protein levels of Cox2, while stable levels of the mitoribosomal protein Mrp20 acted as indirect evidence for intact mtDNA[41,42] (Extended Data Fig. 5a,b). We enriched for these stalled mitoribosome complexes through multistep lysis and sucrose density centrifugation and performed single-particle cryo-EM (Fig. 3b). After initial data processing (Table 1 and Extended Data Fig. 4), focused classification on the subunit interface of mitochondrial monosomes revealed the absence of tRNA in the A-site, with a single tRNA found in either the P-site or the E-site, which is in line with mitoribosomes unable to elongate (Fig. 3c and Extended Data Fig. 5c). After further focused classification and refinement on the SSU, we observed two major classes of mitoribosomes with additional mRNA and protein densities containing clear signatures of PPR domains located at the MCE (Fig. 3d,e and Extended Data Figs. 4c and 5d). Rigid-body fitting of AlphaFold2-predicted[43] structures of PPR-containing TAs and other PPR proteins (Extended Data Fig. 6a) into the extra densities identified the factors bound to these two post-initiation, pre-elongation complexes as Aep3 (Fig. 3d and Extended Data Fig. 6b), the TA for *ATP8*, and a complex of Aep1, Aep2 and Atp25C (Fig. 3e and Extended Data Fig. 6c–e), the TAs for *ATP9*.

Aep3 engages the initiating mitoribosome

The first class, containing 4.9% of the total amount of particles, demonstrated additional density of a single PPR protein located at the MCE in a cryo-EM map with an overall resolution of 3.7 Å (Figs. 3d and 4a and Extended Data Figs. 4c and 5d,e). Aep3 is predicted to consist of a circular array of PPR motifs (Extended Data Fig. 6a), with an overall conformation that could be rigid-body fitted well into the helical PPR densities, sitting perpendicular to the mitoribosome (Figs. 3d and 4a,b and Extended Data Figs. 5d and 6b). However, some loops of Aep3 were less well resolved and unstructured N-terminal (residues 33–52) and C-terminal (residues 531–558) segments were not observed in the density map; hence, they were removed from the final model (Figs. 3d and 4a,b and Extended Data Fig. 7a). Density representing the *ATP8* mRNA was also detected, extending from an E-site bound tRNA to the MCE (Fig. 4a,b). The 5′ UTR of *ATP8* mRNA is seemingly threaded through Aep3 where it interacts with a positively charged RNA-binding pocket formed by the helical array of PPR motifs (Fig. 4b and Extended Data Fig. 7a). EternaFold, a multitask learning model trained on EteRNA project data, predicts an RNA stem loop with three branches just upstream of where the 5′ end of the Aep3–mitoribosome footprint lies[44] (Fig. 2b and Extended Data Fig. 8a). Some of this predicted secondary structure might explain the double-stranded mRNA density occupying the Aep3 RNA-binding pocket (Fig. 4b,d), although the precise RNA sequence could not be unambiguously determined from the mRNA density. The extensive RNA contacts made by the Aep3 PPR motifs at the MCE is in line with the additional RNAse protection of the *ATP8* 5′ UTR upstream of the initiating mitoribosome in the Aep3 sel-mitoRP data (Fig. 2b and Extended Data Fig. 2c). These data, therefore, confirm and expand on the results from Aep3 sel-mitoRP that Aep3 binds to the 5′ UTR of its target transcript and to the MCE, presumably to position *ATP8* mRNA for translation initiation.

Aep3 makes direct contacts with the MCE through the mitoribosomal proteins Mrp51 (bS1m) and Mrp21 (bS21m) (Fig. 4a,c–e). Both Mrp51 and Mrp21 have been implicated in translation initiation as mutations of these proteins suppress translation defects caused by mutations in the 5′ UTRs of *COX2* and *COX3* (ref. 45). Additionally, proximity labeling experiments revealed contacts between Mrp51 and several TAs, indicating that it may serve as a docking site for TA interactions with the yeast mitoribosome[14]. Interestingly, our structure contains an extended C-terminal density for Mrp51 not resolved in previous mitoribosome structures[8,46] (Fig. 4c–e and Extended Data Fig. 7b,d), which presumably forms a contact and binding platform for Aep3. The density for this C-terminal extension was weak, likely representing flexibility of this segment, but ends in a strong tubular density bound to Aep3 in parallel with PPR helices 14 and 16 (Fig. 4c–e and Extended Data Fig. 7a,b). When using Alphafold3 (ref. 38) to predict the structure of a complex between Aep3 and Mrp51, a C-terminal helix of Mrp51 was predicted to bind Aep3 in this exact location (Fig. 4c–e and Extended Data Fig. 7b).

To further investigate the importance of the Mrp51 C-terminal segment for TA binding, we generated strains carrying C-terminal truncations of Mrp51 at residue F308 or R325 (Fig. 4f,g). F308 is close to the last C-terminal residue modeled in previous mitoribosome structures[8,46] (Extended Data Fig. 7d), whereas R325 is located right before the predicted Aep3-interacting C-terminal helix (Fig. 4e). Strikingly, truncation at F308, which removed the last 36 residues of Mrp51, abolished synthesis of Cox1, Cox2, Cox3 and Atp8, whereas synthesis of Var1, Cyt*b*, Atp6 and Atp9 was largely unaffected (Fig. 4h). In contrast, truncation at R325, which removed the C-terminal helix of Mrp51 predicted to interact with Aep3, only abolished synthesis of Atp8, with a modest decrease in Cox2 and Cox3 synthesis (Fig. 4h). These results are in line with our structural work and show that the C terminus of Mrp51 is important for Aep3 binding to the mitoribosome and initiation of *ATP8* translation. Furthermore, it indicates variability in TA binding to the mitoribosomal SSU (mtSSU), where Mrp51 acts as a binding platform for some TAs, whereas some use other modes of interaction.

Fig. 5 | Structure of the *ATP9* TA complex and its interaction with the mitoribosome and 5′ UTR of the mRNA. a, Top view of the mtSSU (yellow), viewed from the intersubunit side, demonstrating the interaction of *ATP9* TAs, Aep1 (light green), Aep2 (forest green) and Atp25C (cyan), with the *ATP9* mRNA (red) at the SSU MCE. SSU protein Mrp1 (orange), Mrp51 (brown) and Rsm26 (yellow) are highlighted. A density for the initiator tRNA (purple) is present in the E-site. **b**, Coimmunoprecipitation (co-IP) of Aep1–FLAG and Aep2–FLAG from whole-cell lysate without crosslinking or RNase treatment. I, input; U, unbound; E, elution. A representative western blot from two biological replicates is shown. **c**, Co-IP of Aep1–FLAG, Aep2–FLAG and Pet111–FLAG from whole-cell lysate demonstrating that Atp25C can be copurified with Aep1 and Aep2 but not with Pet111. A representative western blot from three biological replicates is shown. **d**, Structural model of the *ATP9* TA complex including Aep1 (light green), Aep2 (forest green) and Atp25C (cyan). **e**, Left: structural model of the *ATP9* TA complex in a locally filtered density map with the *ATP9* mRNA density displayed in red. Right: surface map representation of the *ATP9* TA complex highlighting the positively charged residues (blue) that interact with the mRNA. **f**, *ATP9* TA complex and mRNA (red) bound to the SSU MCE highlighted with mitoribosomal proteins Mrp1 (orange), Rsm26 (yellow), Mrp51 (brown) and Mrp21 (light brown). **g**–**i**, Zoomed-in views show the PPR motifs of Aep2 (**g**) and Atp25C (**h**) interacting with ds mRNA segments and Aep1 (**i**) interacting with the SSU proteins Mrp1 and Rsm26. Cryo-EM densities are visualized with maps filtered according to their local resolution, with density thresholds (σ) set to 0.09 for TA proteins and 0.06 for mRNA.

https://doi.org/10.1038/s41594-025-01726-y

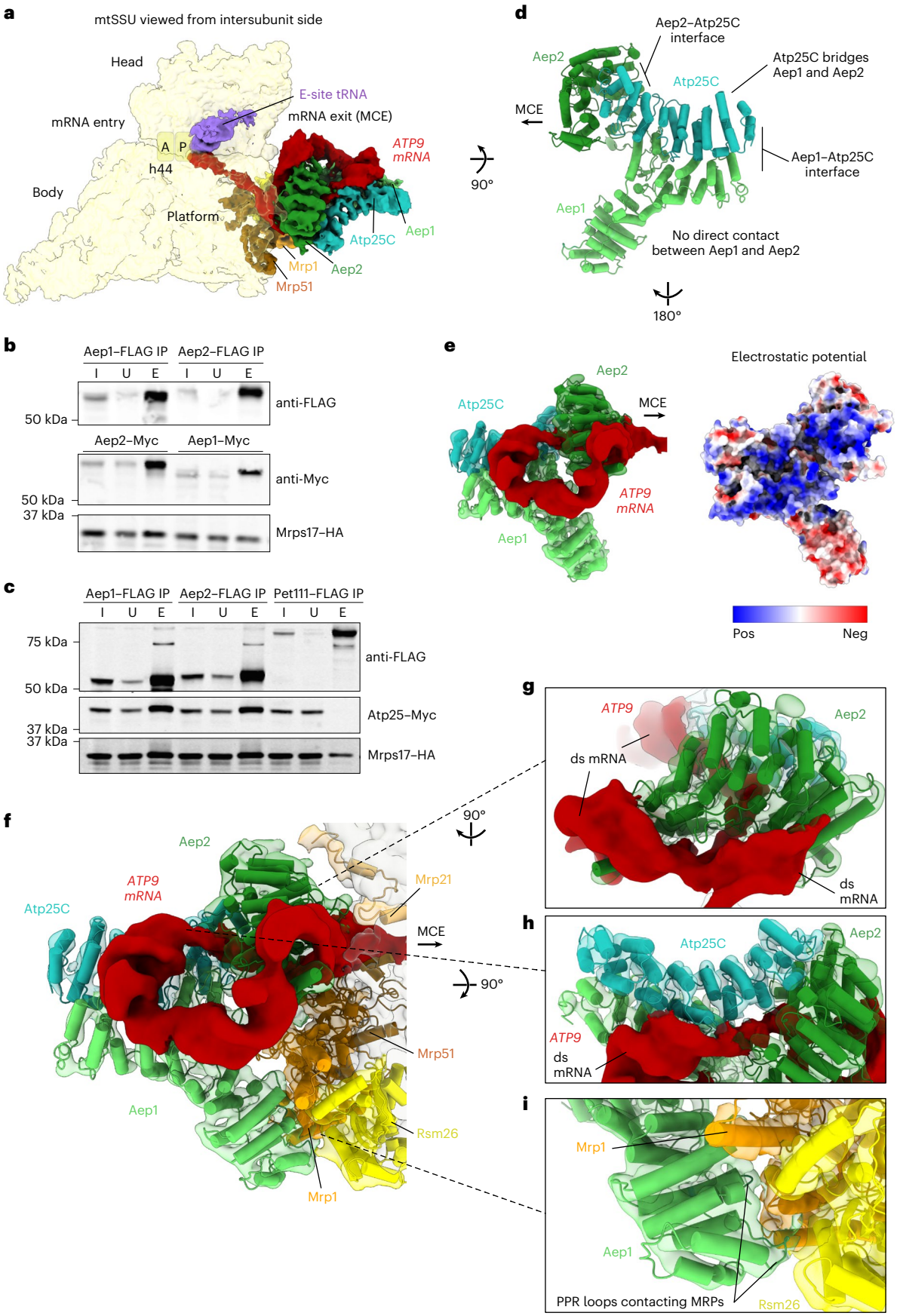

ATP9 TAs bind mitoribosomes at initiation

The other class, obtained from 9.1% of the particles, contained density of a much larger complex bound to the MCE in a map with an overall resolution of 3.8 Å (Figs. 3e and 5a and Extended Data Figs. 4c and 5d,f). Using structure predictions by AlphaFold3 (ref. 38), we tested the rigid-body fit of individual known PPR-containing TAs and other mitochondrial-localized PPR proteins into the density (Extended Data Fig. 6a). This demonstrated that three TAs of *ATP9*, Aep1, Aep2 and Atp25C, had overall conformations that fit well into defined parts of the density (Figs. 3e and 5a,f and Extended Data Fig. 6c–e). For Aep1, the majority of the protein could be fitted into the density, with the exception of N-terminal residues 1–41 corresponding to the predicted mitochondrial targeting signal. For Aep2, residues 1–94 of the N terminus and residues 536–580 of the C terminus did not have a corresponding map density and were, therefore, removed from the model. Atp25, a TA with a role in *ATP9* mRNA stability, is processed upon import into mitochondria with the 36-kDa C-terminal protein (Atp25C) controlling *ATP9* translation[47,48]. Consistently, Atp25C, ranging between residues 296 and 609, fit well into our cryo-EM map.

An independent prediction of a complex consisting of Aep1, Aep2 and Atp25C using AlphaFold3 resulted in a similar structure that fit well into the additional density (Extended Data Fig. 7c). The existence of a single complex containing both Aep1 and Aep2 explains the highly similar sel-mitoRP profiles of Aep1 and Aep2 (Figs. 1d and 2a). To further confirm the composition of the complex, we immunoprecipitated tagged Aep1 or Aep2 from lysates and found that both Aep1 and Aep2 interacted with each other (Fig. 5b). Aep1 and Aep2 but not the *COX2* TA, Pet111, also coimmunoprecipitated Atp25C, supporting a specific complex of Aep1, Aep2 and Atp25C (Fig. 5c). Our structure revealed that Aep1 and Aep2 do not directly contact each other (Fig. 5d). Instead, they are connected by Atp25C, which largely consists of PPR motifs creating a characteristic PPR superhelical groove[49], arching between the two proteins (Fig. 5d). The C terminus of Atp25C is bound to Aep2 while the N-terminal part shares a long interaction surface with Aep1. Aep1 in turn contains an N-terminal bundle of PPR helices (PPR motifs 1–3; Extended Data Fig. 7a) that anchors the TA complex to the mitoribosome by making direct contacts with Rsm26 (mS42) and Mrp1 (mS43) (Fig. 5f,i). Mrp1 is a component of the SSU that is unique to the mitoribosome and has been found to genetically interact with TAs[30]. Similar to Mrp51, proximity labeling experiments showed that Mrp1 is in close contact with several different TAs[14] and may also act as a major binding surface. Aep2, on the other hand, is adjacent to Mrp51 and Mrp21, as well as Mrps18 (uS11m) and Mrp17 (bS6m), but seemingly does not make strong direct contacts with the SSU (Fig. 5a,f and Extended Data Fig. 7e). Aep2 and Atp25C are instead mostly linked to the mitoribosome through their interactions with Aep1 and the 5′ UTR of the mRNA. The PPR domains from each of the three proteins in the heterotrimer come together to form an RNA-binding scaffold (Fig. 5e). We were able to visualize mRNA density extending from the tRNA-binding sites, where the initiator fMet-tRNA presumably base pairs with the AUG start codon, through the mRNA channel to the MCE, where the mRNA exits the mitoribosome and wraps around the TA complex (Fig. 5a,e,f).

TA–mitoribosome structures are consistent with their 5′ UTR footprints

The *ATP9* 5′ UTR footprints that we recovered in the Aep1 and Aep2 sel-mitoRP datasets can be explained by the structure of the *ATP9* TA complex bound to the 5′ UTR (Figs. 1d and 2a). One set of RNA footprints, described above, abut the start codon and are consistent with an initiating mitoribosome bound to the TA complex. This footprint arises from the combined protection of the mitoribosome from the start codon until the MCE and the TA complex, which protects an additional 20 nt upstream (Figs. 2a and 5a). Sel-mitoRP of Aep1 and Aep2 also exhibited footprints approximately 130 nt upstream of the start codon, which initially were unexpected (Figs. 1d and 2a). However, these footprints may be explained by two EternaFold-predicted stem-loop structures between the UTR footprints[44] (Extended Data Fig. 8b), bringing the upstream footprint much closer to the start codon in three-dimensional (3D) space (Fig. 5a,f). Although we could visualize RNA density consistent with double-stranded stem-like structures, we did not visualize the loop portions of the stem loops in our structure, probably because of flexibility of portions of RNA not bound by the TAs (Fig. 5e,f).

Binding of the 5′ UTR of *ATP9* is achieved through a positively charged surface of the Aep1–Aep2–Atp25C complex that is complementary to the mRNA conformation (Fig. 5e). PPR motifs 6 and 8 of Aep1 make contact with the 5′ UTR of *ATP9*, whereas PPR motifs 1–3 of Aep1 do not bind the RNA but instead establish protein–protein contacts with the mitoribosome (Fig. 5f,i and Extended Data Fig. 7a). Furthermore, Atp25C makes extensive contacts with the 5′ UTR through PPR motifs 3–5 (Fig. 5h and Extended Data Fig. 7a). Atp25C thereby forms a bridge between Aep1 and Aep2 through its protein–protein and protein–RNA interactions relying on its PPR repeats (Fig. 5d,h and Extended Data Fig. 7a). Aep2 localizes adjacent to the MCE and makes the most contacts with the 5′ UTR through PPR motifs 1, 2, 5 and 6, including an RNA loop positioned between Aep2 and the surface of the mitoribosome (Fig. 5a,f,g). It is possible that this RNA loop contributes to the selectivity of Aep2 in recognizing and binding the *ATP9* mRNA to guide the mitoribosome to the correct start codon during initiation. Together, Aep1 and Aep2 sel-mitoRP and the *ATP9* TA–mitoribosome structure demonstrate that the *ATP9* TAs link the *ATP9* 5′ UTR and the MCE to position the *ATP9* mRNA for initiation.

ATP9 TAs interact with the mitoribosomes during translation initiation and before elongation

Atp9 biogenesis is special, as it requires the assembly of ten identical subunits into a ring structure, which is the central part of the rotor component of ATP synthase. A possible scenario is that *ATP9* mRNA is translated by the same mitoribosome over and over to produce many copies of the protein to facilitate assembly. This in turn could be aided by a more constant binding of the *ATP9* TA complex to the ribosome. To test this, we next asked whether the complex is directly released from the mitoribosome upon commencement of translation elongation or whether it stays bound longer. To address this question, we performed affinity purification of Aep2-bound

Table 2 | Cryo-EM data collection, refinement and validation statistics (Aep2-bound yeast mitochondrial ribosome)

	LSU (EMD-48390)	SSU (EMD-48388)	Aep1–Aep2–Atp25C (EMD-48387)
Data collection and processing			
Magnification	105,000	105,000	105,000
Voltage (kV)	300	300	300
Electron exposure (e^- per Å^2)	48.5	48.5	48.5
Defocus range (μm)	−0.8 to −2.0	−0.8 to −2.0	−0.8 to −2.0
Pixel size (Å)	1.19	1.19	1.19
Symmetry imposed	C_1	C_1	C_1
Initial particle images (no.)	874,238	874,238	874,238
Final particle images (no.)	61,709	70,511	25,098
Map resolution (Å)	2.9	3.6	4.4
FSC threshold	0.143	0.143	0.143
Map resolution range (Å)	2.5–5.0	2.5–6.5	4.0–7.0

https://doi.org/10.1038/s41594-025-01726-y

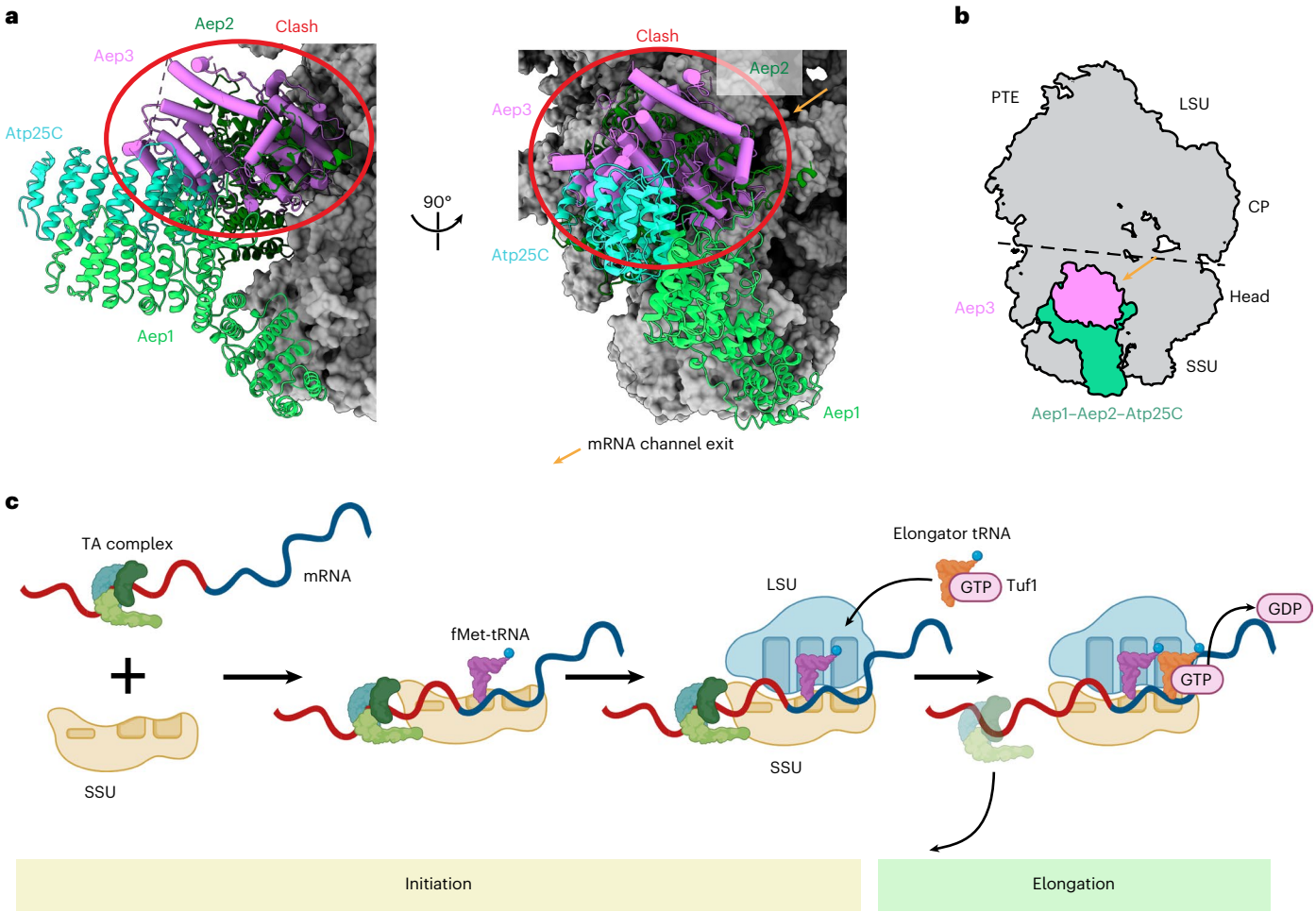

Fig. 6 | TA complexes preferentially engage with initiating mitoribosomes to position their target mRNA for translation initiation. a, Overlay of the structural models from this study: *ATP9* TA complex (Aep1, light green; Aep2, forest green; Atp25C, cyan) shown in ribbon representation and *ATP8* TA (Aep3, lavender) shown in tube representation, with a previously published apo yeast mitoribosome structure (PDB 5MRC, gray), shown in surface representation. The different structures of mitoribosomes are aligned on the ribosome core, with the position of the TA complexes shown in two different orientations. The area of clash between the two TA complexes is highlighted with a red circle and the MCE is indicated with an orange arrow. **b**, Cartoon representation showing the overlapping location of the two TA complexes on the mtSSU. The MCE is indicated with an orange arrow. **c**, Model of mRNA recruitment and positioning by the TA complexes in yeast mitochondria. The dedicated TA complex engages with the 5′ UTR of its target transcript and the SSU, positioning the start codon within the P-site of the SSU. The TA complex then departs the mitoribosome during early translation elongation. Panel **c** created with BioRender.com.

mitoribosomes from an Aep2–3×FLAG-tagged strain actively respiring and translating (Extended Data Figs. 9 and 10). Cryo-EM analysis of these Aep2 mitoribosome particles yielded a prevailing class showing a highly similar density map to the *ATP9* TA–mitoribosome complex described above (Table 2 and Extended Data Figs. 9 and 10b,c). Indeed, overlay of the TA-bound SSU from these two cryo-EM datasets revealed that the TA complex made nearly identical interactions with the mitoribosome (Extended Data Fig. 10d), with a minor rearrangement of the tRNA bound (Extended Data Fig. 10e).

Our overlapping structures of the *ATP9* TA complex obtained through orthogonal means indicate that the *ATP9* TAs bind only at early stages of translation to newly initiating mitoribosomes, consistent with sel-mitoRP data showing a rapid depletion of Aep1 and Aep2 from the mitoribosome after initiation (Fig. 1d). Moreover, aligning our structures with an apo yeast mitoribosome structure[8] (Protein Data Bank (PDB) 5MRC) revealed that the binding sites of Aep3 (*ATP8* TA) and Aep1–Aep2–Atp25C (*ATP9* TAs) near the MCE are mutually exclusive (Fig. 6a,b and Extended Data Fig. 7e). This supports the selective action of each TA in facilitating the translation initiation of specific mitochondrial transcripts (Fig. 6c), as indicated by our selective mitoribosome profiling data.

Discussion

The faithful choice of the start codon by ribosomes is key for correctly identifying and reading the intended open reading frame during protein synthesis. Here, we identified how TAs support this key step during translation initiation in yeast mitochondria. The combination of sel-mitoRP analyses and cryo-EM structures demonstrated that TAs bind specifically to their target transcript and to the mtSSU to position the start codon in the P-site of the mitoribosome for translation initiation (Fig. 6c). The TAs bind to their target transcripts in the 5′ UTR approximately 30 nt upstream of the start codon (Fig. 2). The precise position of the TA binding is likely aided by predicted RNA secondary structures around the binding sites and determines the distance between the TA binding site and the start codon (Extended Data Fig. 8). Binding of the TAs to the MCE then allows for the alignment of the mRNA into the mRNA channel for translation initiation. Accordingly, mitochondrial TAs replace the molecular function of the SD mechanism, which is used by the ancestral bacterial system.

TAs were identified early during the genetic mapping of genes affecting mitochondrial functions and were later shown to have crucial roles for translation of individual mitochondrial-encoded mRNAs. Through their molecular function during initiation, they not

only are necessary for mitochondrial translation but also have key roles in organizing and regulating mitochondrial protein synthesis[6]. Data obtained over the years have suggested that TAs can also localize the synthesis of specific OXPHOS subunits to distinct sites in the inner membrane to presumably increase assembly efficiency[50,51]. Likewise, mitochondrial translation of OXPHOS proteins must be carefully coordinated with synthesis of nuclear-encoded OXPHOS subunits to ensure the stoichiometric assembly of OXPHOS complexes[2]. Recent work demonstrated that *COB* translation is regulated by a feedback loop that depends on the influx of nuclear-encoded subunits and maintains the balance between nuclear-encoded and mitochondrial-encoded subunits of complex III (refs. 17,18). Interestingly, Cbp1, which has been shown to be involved in this feedback loop, associated with mitoribosomes during *COB* translation initiation but was not as selectively enriched on its target transcript as the other PPR TAs (Fig. 1c,d). This finding agrees with previous work showing that *COB* TAs can bind to the mitoribosome even in the absence of *COB* mRNA, arguing that *COB* TAs are bound to the mitoribosome even when not actively participating in translational activation[18]. Consistently, *COB* TAs engage with the mitoribosome through the large subunit (LSU) of the mitoribosome, whereas our structures for the *ATP9* and *ATP8* TAs show that they bind to the SSU. Additionally, Cbp1 is found in a high-molecular-weight complex with Pet309, a *COX1* TA[52]. In agreement with these data, we saw a strong enrichment peak for Cbp1 in the 5′ UTR of *COX1* that overlapped with the Pet309 binding peak (Fig. 1c). The differences in how Cbp1 and potentially the other *COB* TAs engage with the mitoribosome argue that *COB* translation is regulated differently than other mitochondrial mRNAs[53].

Functional genetic studies have implied that TAs interact directly with the mitoribosome and the 5′ UTR of their target transcript; however, biochemical and structural evidence of these interactions was lacking. The first cryo-EM structure of the yeast mitoribosome found an unresolved density at the extended MCE containing mitoribosomal-specific proteins[8]. It was proposed that this density was a heterogeneous mixture of TAs and that the MCE of the yeast mitoribosome could serve as a docking platform for TAs. Consistently, several TAs, including Aep1 and Pet111, were shown to populate the MCE by proximity labeling proteomics[14]. Our structural analysis of initiating mitoribosomes determined that the *ATP9* TAs (Aep1, Aep2 and Atp25C) form a heterotrimer that mainly binds to the mitoribosomal protein Mrp1 at the MCE (Fig. 5f,i). The structure of Aep3 bound to an initiating mitoribosome revealed that it binds to the mitoribosome mainly through Mrp51 (Fig. 4c). Our in vivo labeling experiments further showed that truncating the C-terminal end of Mrp51 prevented translation of several mitochondrial transcripts (Fig. 4h), indicating the importance of Mrp51 for binding of other TAs. Hence, these data demonstrate that the expanded MCE of the yeast mitoribosome, which contains Mrp1 and Mrp51, serves as an overall docking site for the yeast TAs. Interestingly, in bacteria the homolog of Mrp51, bS1, was also shown to be important for translation initiation by establishing an initial contact between the ribosome and incoming mRNA[54].

Our cryo-EM structures revealed how TAs engage with the mRNA during translation initiation through direct binding of the *ATP9* and *ATP8* 5′ UTRs by their respective TAs (Figs. 4 and 5), which corresponded well with the footprints identified near the start codons of those transcripts (Fig. 2a,b). Indeed, we found that most of the TA–mitoribosome complexes exhibited footprints just upstream of the start codon that are likely because of the RNA protection afforded by TAs at their binding sites. Mitochondrial TAs must adapt to meet the needs of the divergent mitochondrial transcriptomes across species. Plant PPR proteins bind RNA in a sequence-specific manner dictated by the plant PPR code, whereby residues located in the loops between the two α-helices in the PPR motif are used to decipher a specific nucleotide in an RNA sequence[55,56]. Sel-mitoRP data from this study indicate that most of the yeast PPR TAs bind their target mRNAs with high selectivity. Given that mitochondrial UTRs have a highly enriched A+U content, it is unlikely that PPR binding follows a strict sequence-specific RNA-binding mode. Indeed, the structures of TA–mitoribosome complexes with bound mRNA show that 5′ UTR binding by PPR proteins involves not only single-strand interactions but also the recognition of more complex secondary structures including double strands that presumably bring together annealing sequences spread on the RNA in 3D space (Figs. 4b–d and 5a,e–h and Extended Data Fig. 8a,b). These interactions would be in line with the TA–mitoribosome footprints further upstream for *ATP9, COX1* and *COB* (Fig. 2a,c)[53]. Moreover, a T-to-C conversion at −16 in the *ATP9* 5′ UTR rescues a temperature sensitive allele of Aep2 (ref. 57) and is predicted to disrupt the putative stem loop that forms upstream of the start codon that would sterically prevent ribosome binding (Extended Data Fig. 8c). Of note, we found that PPR motifs of these TAs do not exclusively interact with RNA but are also involved in establishing protein–protein contacts, for example, between the components of the *ATP8* TA or *ATP9* TA complex to the mitoribosome (Figs. 4c and 5i). How RNA structure impacts TA binding and mitoribosome initiation represents an interesting future direction.

Evolution of the human mitochondrial genome has led to the complete loss of 5′ UTRs on protein-coding transcripts, such that, if TAs exist for each human mitochondrial transcript, they have changed so much in structure and function from their yeast counterparts as to be unrecognizable. TACO1 was initially assumed to be a TA of mammalian *COX1* (ref. 58); however, it was recently shown to act during translation elongation[59]. LRPPRC, a mammalian PPR protein, binds to the mitoribosome at the mRNA channel entrance and impacts translational efficiency of several mitochondrial transcripts[60] through a yet poorly understood mechanism. Future work performing sel-mitoRP for LRPPRC and other putative translational regulators in human mitochondria will be important to understand how mitochondrial translation has adapted in response to the loss of the regulatory 5′ UTRs that are so critical for translation initiation in yeast. This approach will provide crucial insights into the evolutionary strategies used to maintain efficient and specific mitochondrial translation across diverse eukaryotic lineages.

Online content

Any methods, additional references, Nature Portfolio reporting summaries, source data, extended data, supplementary information, acknowledgements, peer review information; details of author contributions and competing interests; and statements of data and code availability are available at https://doi.org/10.1038/s41594-025-01726-y.

References

1. Lipinski, K. A., Kaniak-Golik, A. & Golik, P. Maintenance and expression of the *S. cerevisiae* mitochondrial genome—from genetics to evolution and systems biology. *Biochim. Biophys. Acta* **1797**, 1086–1098 (2010).
2. Couvillion, M. T., Soto, I. C., Shipkovenska, G. & Churchman, L. S. Synchronized mitochondrial and cytosolic translation programs. *Nature* **533**, 499–503 (2016).
3. Soto, I. et al. Balanced mitochondrial and cytosolic translatomes underlie the biogenesis of human respiratory complexes. *Genome Biol.* **23**, 170 (2022).
4. Khalimonchuk, O., Bird, A. & Winge, D. R. Evidence for a pro-oxidant intermediate in the assembly of cytochrome oxidase. *J. Biol. Chem.* **282**, 17442–17449 (2007).
5. Kremer, L. S. & Rehling, P. Coordinating mitochondrial translation with assembly of the OXPHOS complexes. *Hum. Mol. Genet.* **33**, R47–R52 (2024).
6. Fox, T. D. Mitochondrial protein synthesis, import, and assembly. *Genetics* **192**, 1203–1234 (2012).
7. Ban, N., Nissen, P., Hansen, J., Moore, P. B. & Steitz, T. A. The complete atomic structure of the large ribosomal subunit at 2.4 Å resolution. *Science* **289**, 905–920 (2000).

8. Desai, N., Brown, A., Amunts, A. & Ramakrishnan, V. The structure of the yeast mitochondrial ribosome. *Science* **355**, 528–531 (2017).
9. Wimberly, B. T. et al. Structure of the 30S ribosomal subunit. *Nature* **407**, 327–339 (2000).
10. Schluenzen, F. et al. Structure of functionally activated small ribosomal subunit at 3.3 Å resolution. *Cell* **102**, 615–623 (2000).
11. Bieri, P., Greber, B. J. & Ban, N. High-resolution structures of mitochondrial ribosomes and their functional implications. *Curr. Opin. Struct. Biol.* **49**, 44–53 (2018).
12. Rodnina, M. V. Translation in prokaryotes. *Cold Spring Harb. Perspect. Biol.* **10**, a032664 (2018).
13. Herrmann, J. M., Woellhaf, M. W. & Bonnefoy, N. Control of protein synthesis in yeast mitochondria: the concept of translational activators. *Biochim. Biophys. Acta* **1833**, 286–294 (2013).
14. Singh, A. P. et al. Molecular connectivity of mitochondrial gene expression and OXPHOS biogenesis. *Mol. Cell* **79**, 1051–1065 (2020).
15. Perez-Martinez, X., Butler, C. A., Shingu-Vazquez, M. & Fox, T. D. Dual functions of Mss51 couple synthesis of Cox1 to assembly of cytochrome c oxidase in *Saccharomyces cerevisiae* mitochondria. *Mol. Biol. Cell* **20**, 4371–4380 (2009).
16. Mick, D. U. et al. Coa3 and Cox14 are essential for negative feedback regulation of *COX1* translation in mitochondria. *J. Cell Biol.* **191**, 141–154 (2010).
17. Gruschke, S. et al. The Cbp3–Cbp6 complex coordinates cytochrome *b* synthesis with bc_1 complex assembly in yeast mitochondria. *J. Cell Biol.* **199**, 137–150 (2012).
18. Salvatori, R. et al. Molecular wiring of a mitochondrial translational feedback loop. *Mol. Cell* **77**, 887–900 (2019).
19. Lipinski, K. A., Puchta, O., Surendranath, V., Kudla, M. & Golik, P. Revisiting the yeast PPR proteins—application of an iterative hidden Markov model algorithm reveals new members of the rapidly evolving family. *Mol. Biol. Evol.* **28**, 2935–2948 (2011).
20. Manthey, G. M. & McEwen, J. E. The product of the nuclear gene *PET309* is required for translation of mature mRNA and stability or production of intron-containing RNAs derived from the mitochondrial *COX1* locus of *Saccharomyces cerevisiae*. *EMBO J.* **14**, 4031–4043 (1995).
21. Barros, M. H. & Tzagoloff, A. Aep3p-dependent translation of yeast mitochondrial ATP8. *Mol. Biol. Cell* **28**, 1426–1434 (2017).
22. Zeng, X., Hourset, A. & Tzagoloff, A. The *Saccharomyces cerevisiae ATP22* gene codes for the mitochondrial ATPase subunit 6-specific translation factor. *Genetics* **175**, 55–63 (2007).
23. Islas-Osuna, M. A., Ellis, T. P., Marnell, L. L., Mittelmeier, T. M. & Dieckmann, C. L. Cbp1 is required for translation of the mitochondrial cytochrome *b* mRNA of *Saccharomyces cerevisiae*. *J. Biol. Chem.* **277**, 37987–37990 (2002).
24. Payne, M. J., Finnegan, P. M., Smooker, P. M. & Lukins, H. B. Characterization of a second nuclear gene, *AEP1*, required for expression of the mitochondrial OLI1 gene in *Saccharomyces cerevisiae*. *Curr. Genet.* **24**, 126–135 (1993).
25. Finnegan, P. M., Payne, M. J., Keramidaris, E. & Lukins, H. B. Characterization of a yeast nuclear gene, *AEP2*, required for accumulation of mitochondrial mRNA encoding subuuit 9 of the ATP synthase. *Curr. Genet.* **20**, 53–61 (1991).
26. Steele, D. F., Butler, C. A. & Fox, T. D. Expression of a recoded nuclear gene inserted into yeast mitochondrial DNA is limited by mRNA-specific translational activation. *Proc. Natl Acad. Sci. USA* **93**, 5253–5257 (1996).
27. Zamudio-Ochoa, A., Camacho-Villasana, Y., García-Guerrero, A. E. & Pérez-Martínez, X. The Pet309 pentatricopeptide repeat motifs mediate efficient binding to the mitochondrial *COX1* transcript in yeast. *RNA Biol.* **11**, 953–967 (2014).
28. Jones, J. L. et al. Yeast mitochondrial protein Pet111p binds directly to two distinct targets in *COX2* mRNA, suggesting a mechanism of translational activation. *J. Biol. Chem.* **294**, 7528–7536 (2019).
29. Herbert, C. J., Golik, P. & Bonnefoy, N. Yeast PPR proteins, watchdogs of mitochondrial gene expression. *RNA Biol.* **10**, 1477–1494 (2013).
30. Haffter, P., McMullin, T. W. & Fox, T. D. Functional interactions among two yeast mitochondrial ribosomal proteins and an mRNA-specific translational activator. *Genetics* **127**, 319–326 (1991).
31. Wagner, S. et al. Selective translation complex profiling reveals staged initiation and co-translational assembly of initiation factor complexes. *Mol. Cell* **79**, 546–560 (2020).
32. Galmozzi, C. V., Merker, D., Friedrich, U. A., Döring, K. & Kramer, G. Selective ribosome profiling to study interactions of translating ribosomes in yeast. *Nat. Protoc.* **14**, 2279–2317 (2019).
33. Poutre, C. G. & Fox, T. D. *PET111*, a *Saccharomyces cerevisiae* nuclear gene required for translation of the mitochondrial mRNA encoding cytochrome c oxidase subunit II. *Genetics* **115**, 637–647 (1987).
34. Mulero, J. J. & Fox, T. D. PET111 acts in the 5′-leader of the *Saccharomyces cerevisiae* mitochondrial *COX2* mRNA to promote its translation. *Genetics* **133**, 509–516 (1993).
35. Ferguson, L. et al. Streamlined and sensitive mono- and di-ribosome profiling in yeast and human cells. *Nat. Methods* **20**, 1704–1715 (2023).
36. Lareau, L. F., Hite, D. H., Hogan, G. J. & Brown, P. O. Distinct stages of the translation elongation cycle revealed by sequencing ribosome-protected mRNA fragments. *eLife* **3**, e01257 (2014).
37. Wu, C. C.-C., Zinshteyn, B., Wehner, K. A. & Green, R. High-resolution ribosome profiling defines discrete ribosome elongation states and translational regulation during cellular stress. *Mol. Cell* **73**, 959–970 (2019).
38. Abramson, J. et al. Accurate structure prediction of biomolecular interactions with AlphaFold 3. *Nature* **630**, 493–500 (2024).
39. Rosenthal, L. P. & Bodley, J. W. Purification and characterization of *Saccharomyces cerevisiae* mitochondrial elongation factor Tu. *J. Biol. Chem.* **262**, 10955–10959 (1987).
40. Zeng, R., Smith, E. & Barrientos, A. Yeast mitoribosome large subunit assembly proceeds by hierarchical incorporation of protein clusters and modules on the inner membrane. *Cell Metab.* **27**, 645–656 (2018).
41. Fearon, K. & Mason, T. L. Structure and function of *MRP20* and *MRP49*, the nuclear genes for two proteins of the 54 S subunit of the yeast mitochondrial ribosome. *J. Biol. Chem.* **267**, 5162–5170 (1992).
42. Jia, L. et al. Yeast Oxa1 interacts with mitochondrial ribosomes: the importance of the C-terminal region of Oxa1. *EMBO J.* **22**, 6438–6447 (2003).
43. Jumper, J. et al. Highly accurate protein structure prediction with AlphaFold. *Nature* **596**, 583–589 (2021).
44. Wayment-Steele, H. K., Kladwang, W., Strom, A. I. & Das, R. RNA secondary structure packages evaluated and improved by high-throughput experiments. *Nat. Methods* **19**, 1234–1242 (2022).
45. Green-Willms, N. S., Fox, T. D. & Costanzo, M. C. Functional interactions between yeast mitochondrial ribosomes and mRNA 5′ untranslated leaders. *Mol. Cell. Biol.* **18**, 1826–1834 (1998).
46. Ast, T. et al. METTL17 is an Fe–S cluster checkpoint for mitochondrial translation. *Mol. Cell* **84**, 359–374 (2024).
47. Woellhaf, M. W., Sommer, F., Schroda, M. & Herrmann, J. M. Proteomic profiling of the mitochondrial ribosome identifies Atp25 as a composite mitochondrial precursor protein. *Mol. Biol. Cell* **27**, 3031–3039 (2016).
48. Zeng, X., Barros, M. H., Shulman, T. & Tzagoloff, A. *ATP25*, a new nuclear gene of *Saccharomyces cerevisiae* required for expression and assembly of the Atp9p subunit of mitochondrial ATPase. *Mol. Biol. Cell* **19**, 1366–1377 (2008).

49. Manna, S. An overview of pentatricopeptide repeat proteins and their applications. *Biochimie* **113**, 93–99 (2015).
50. Naithani, S., Saracco, S. A., Butler, C. A. & Fox, T. D. Interactions among *COX1*, *COX2*, and *COX3* mRNA-specific translational activator proteins on the inner surface of the mitochondrial inner membrane of *Saccharomyces cerevisiae*. *Mol. Biol. Cell* **14**, 324–333 (2003).
51. Stoldt, S. et al. Spatial orchestration of mitochondrial translation and OXPHOS complex assembly. *Nat. Cell Biol.* **20**, 528–534 (2018).
52. Krause, K., Lopes de Souza, R., Roberts, D. G. W. & Dieckmann, C. L. The mitochondrial message-specific mRNA protectors Cbp1 and Pet309 are associated in a high-molecular weight complex. *Mol. Biol. Cell* **15**, 2674–2683 (2004).
53. Carlström, A. et al. A molecular switch at the yeast mitoribosomal tunnel exit controls cytochrome *b* synthesis. *Nucleic Acids Res* **53**, gkaf634 (2025).
54. Webster, M. W. et al. Molecular basis of mRNA delivery to the bacterial ribosome. *Science* **386**, eado8476 (2024).
55. Barkan, A. et al. A combinatorial amino acid code for RNA recognition by pentatricopeptide repeat proteins. *PLoS Genet.* **8**, e1002910 (2012).
56. Yin, P. et al. Structural basis for the modular recognition of single-stranded RNA by PPR proteins. *Nature* **504**, 168–171 (2013).
57. Ellis, T. P., Lukins, H. B., Nagley, P. & Corner, B. E. Suppression of a nuclear *aep2* mutation in *Saccharomyces cerevisiae* by a base substitution in the 5′-untranslated region of the mitochondrial oli1 gene encoding subunit 9 of ATP synthase. *Genetics* **151**, 1353–1363 (1999).
58. Weraarpachai, W. et al. Mutation in *TACO1*, encoding a translational activator of COX I, results in cytochrome c oxidase deficiency and late-onset Leigh syndrome. *Nat. Genet.* **41**, 833–837 (2009).
59. Brischigliaro, M. et al. The human mitochondrial translation factor TACO1 alleviates mitoribosome stalling at polyproline stretches. *Nucleic Acids Res.* **52**, 9710–9726 (2024).
60. Singh, V. et al. Structural basis of LRPPRC–SLIRP-dependent translation by the mitoribosome. *Nat. Struct. Mol. Biol.* **31**, 1838–1847 (2024).

Methods

Yeast strain construction

Gene tagging and deletion was performed using standard transformation of PCR products[61]. All transformants were verified by colony PCR and western blotting. Epitope tags were introduced at the 3′ end of the endogenous locus using a scarless loopout method[62,63].

For the strain with mitoribosomes stalled at initiation, a *kanMX* cassette was used to delete *TUF1* in a W303 strain background carrying the plasmids YEplac181-*RNR1* (*LEU2* selection) and pRS316-*VAR1* (*URA3* selection)[40]. The same strain background was used to generate the Mrp51 truncation mutants, where an ALFA epitope tag[64] was added to the C terminus using a *cloNAT* selection cassette. All strains, plasmids and primers used to generate the strains in this study are listed in Supplementary Tables 1–3, respectively.

Western blotting and antibodies

First, 5× SDS–PAGE loading buffer was added to samples at a final concentration of 1× and samples were boiled for 5 min at 95 °C before loading onto NuPAGE Bis–Tris gels (Invitrogen). Protein transfer to a nitrocellulose membrane was carried out using a Trans-Blot Turbo (Bio-Rad) and the membranes were blocked in 5% milk in TBST (0.1% Tween-20). Then, 3×FLAG-tagged proteins were detected with mouse anti-FLAG (Millipore-Sigma, F1804, 1:1,000), 3×HA-tagged proteins were detected using mouse anti-HA (Invitrogen, 26183, 1:1,000) and 3×Myc-tagged proteins were detected using mouse anti-Myc (Millipore-Sigma, 05-724, 1:500). IRDye 800CW goat anti-mouse secondary antibodies (LICORbio, 925-32210, 1:5,000) were used to image protein bands on a LICOR machine. Rabbit antibodies used in this study included anti-Mrp20 (ref. 65), anti-Mrpl4 (ref. 65), anti-Mrpl36 (ref. 66), anti-Cox2 (W. Neupert lab, Ludwig Maximilian University of Munich), anti-Tom70 (D. Rapaport lab, University of Tübingen), anti-Tuf1 (this study) and anti-ALFA (NanoTag Biotechnologies, N1580). The antibody to Tuf1 was obtained by immunizing rabbits with purified mature Tuf1. All rabbit antibodies were detected using goat anti-rabbit IgG H+L–horseradish peroxidase conjugate (Bio-Rad, 1706515).

Selective mitoribosome profiling

Yeast were grown in YPGal (1% yeast extract, 2% peptone, 2% galactose) pH 5.0 until an optical density at 600 nm (OD_{600}) of approximately 1. Then, 150 ml of culture was snap-chilled before formaldehyde crosslinking by pouring the culture into a prechilled 500-ml centrifuge bottle filled with 50 g of frozen, crushed ice cubes made from MilliQ water. The culture was quickly swirled in the centrifuge bottle and placed on ice. Next, 10 ml of 16% formaldehyde was added to the chilled culture and the crosslinking proceeded for 1 h on ice with swirling every 15 min. Then, 11 ml of 2.5 M glycine was added to the culture to quench the crosslinking reaction. The culture was then pelleted and washed twice in 40 ml of ice-cold crosslinking wash buffer (50 mM HEPES pH 7.5, 50 mM NH_4Cl and 10 mM $MgCl_2$). The pellet was then resuspended in 4 ml of crosslinking lysis buffer (50 mM HEPES pH 7.5, 50 mM NH_4Cl, 10 mM $MgCl_2$, 1.5× cOmplete EDTA-free protease inhibitor cocktail and 0.5% lauryl maltoside) and dripped into a 50-ml conical flask filled with liquid nitrogen to form frozen droplets.

The frozen cells with lysis buffer were then mechanically lysed using liquid-nitrogen-chilled 50-ml canisters for six cycles of 3 min at 15 Hz using a Retsch MM301 mixer mill. The canisters were chilled in liquid nitrogen in between cycles to keep the cells frozen during the lysis. The frozen cell powder was transferred to a 50-ml conical flask and thawed in a water bath at room temperature. The thawed cell lysate was diluted with 2 ml of fresh crosslinking lysis buffer.

To isolate ribosome-protected RNA fragments, the lysates were treated with 300 U of RNase I (Epicentre) for 30 min in a water bath at room temperature, swirling halfway to mix. Then, 600 U of SUPERase-In RNase inhibitor was added to the lysate to stop RNase digestion. The RNase-treated lysate was then centrifuged at 3,000 rpm (1,744*g*) for 5 min at 4 °C. The cleared lysate was then further clarified by transferring to 1.5-ml tubes and centrifuging for 15 min at 20,000*g* at 4 °C. Next, 3.5 ml of the clarified lysate was layered on top of 8 ml of sucrose cushion buffer (50 mM HEPES pH 7.5, 50 mM NH_4Cl, 10 mM $MgCl_2$, 1.5× cOmplete EDTA-free protease inhibitor cocktail (Roche) and 24% sucrose). The lysate was then pelleted through the sucrose cushion to isolate ribosomes by centrifuging for 4.5 h in an SW41 Ti rotor at 40,000 rpm (274,000*g*) at 4 °C.

The sucrose cushion and cleared lysate were then removed and the ribosome pellet was resuspended in chilled mitoribosome wash buffer (50 mM HEPES pH 7.5, 50 mM NH_4Cl, 10 mM $MgCl_2$ and 0.1% Triton X-100) overnight at 4 °C with shaking.

The ribosome pellet was further resuspended by pipetting up and down several times and transferred to a 1.5-ml tube. The pellet was then incubated for 30 min at 4 °C with end-over-end rotation to ensure that the pellet was well resuspended. The pellet was then centrifuged at 20,000*g* for 10 min to remove any insoluble residue. The clarified ribosome mixture was then added to 50 µl of packed anti-FLAG M2 affinity gel (Millipore-Sigma) and incubated with end-over-end rotation for 3 h at 4 °C. The resin was then washed three times with 1 ml of cold mitoribosome wash buffer. Following the last wash, the resin was resuspended with 1 ml of mitoribosome wash buffer using a cut pipette tip and transferred to a fresh 1.5-ml tube. The wash was removed and the resin was resuspended in 600 µl of mitoribosome wash buffer with 200 µg ml^{-1} 3×FLAG peptide (Millipore-Sigma). The resin was then incubated for 1 h at 4 °C with rotation. To recover the elution, the resin slurry was passed over a Co-Star SpinX column for 1 min at 16,000*g*. The elution was then transferred to a fresh 1.5-ml tube.

To reverse the formaldehyde crosslinking, 30 µl of 20% SDS, 32 µl of 100 mM DTT and 14 µl of 0.5 M EDTA were added to the elution, which was then heated for 45 min at 70 °C. The RNA footprints were extracted following reversal of the crosslinking using an equal volume of acid–phenol chloroform. Ribosome footprints were then isolated and a complementary DNA library was prepared for Illumina short-read sequencing as previously described[67].

Selective ribosome profiling data analysis

Reads were trimmed to remove ligated 3′ linker (CTGTAGGCACCA TCAAT) with Cutadapt (version 1.14)[68]. Reads without linker were discarded and the unique molecular identifier (UMI, consisting of four random nucleotides introduced at the 5′ end with the reverse transcription primer and ten random nucleotides introduced at the 3′ end with the linker) was then extracted from remaining reads using a custom script. For all Aep1 and Aep2 samples, synthetic RNA oligos of 40 and 33 nt (UAACAACAUUCAUUAUGAAUGAUGUACCAACAC-CUUAUGC and UAACAACAUUCAUUAUGAAUGAUGUACCAACAC) were used as size markers in a separate gel lane during mitoribosome footprint size selection. Reads arising from migrating synthetic oligos were removed in silico using BBTools BBDuk (https://sourceforge.net/projects/bbmap/) with a *k*-mer length of 30. Reads mapping to abundant noncoding RNAs (rRNA and tRNA) were filtered out after alignment using bowtie1 (version 1.2.1.1)[69]. Remaining reads were aligned to the *S. cerevisiae* genome assembly R64 (UCSC: sacCer3) using STAR (version 2.7.3a)[70]. PCR duplicates were identified by their UMI and removed using a custom script. Ribosome A-site positions were determined using an offset from the 3′ end of each read, depending on its length: 37:[−15], 38:[−16], 39:[−17], 40:[−17], 41:[−17]. Shorter read lengths with ambiguous offsets were omitted.

Unless otherwise noted, read counts at each A-site position were summed across replicates (2–6 replicates for each sample) and normalized by total mitochondrial mRNA mapping reads (reads per million mapped reads, RPM). Enrichment over total mitoribosomes was then calculated by summing RPM values in a sliding 9-nt window and dividing by the corresponding sum in the total (Mrps17) dataset. A threshold was set such that, if more than three positions had no

coverage in either sample, the enrichment value was set to 0. This was to avoid spurious signal because of low coverage. G+C content was calculated for a sliding 6-nt window.

In vivo radiolabeling

In vivo labeling of mitochondrially encoded translation products was performed according to the same procedure as previously described[71]. In short, cells were grown in selective minimal medium containing 2% galactose (SGal), 0.5% glucose, adenine and all necessary amino acids except leucine. Cells were harvested in logarithmic growth phase (OD_{600} of 1–2) and then washed once in water and once in SGal medium without amino acids, before being resuspended in SGal with all amino acids except methionine. After incubation for 5 min at 30 °C and 600 rpm, cycloheximide (200 µg ml^{-1}) was added to block cytosolic translation, before the addition of [^{35}S]methionine. Aliquots were taken after 5, 10 and 15 min, to which 10 mM of unlabeled methionine was added. Proteins were extracted by trichloroacetic acid (TCA) precipitation and analyzed with SDS–PAGE using an 18% gel followed by autoradiography.

Mitochondrial isolation and preparation of *tuf1Δ* mitoribosomes

Mitochondria were isolated according to a previously established protocol[72]. In short, yeast was cultured in 8 l of synthetic medium containing 1.7 g l^{-1} yeast nitrogen base, 5 g l^{-1} $(NH_4)_2SO_4$, 20 µg ml^{-1} adenine, uracil and arginine, 15 µg ml^{-1} histidine and 30 µg ml^{-1} lysine, supplemented with 2% glucose. Cells were grown overnight at 30 °C and 170 rpm to an OD_{600} of 3 before harvesting at 3,000*g* for 5 min, washed with distilled water and resuspended in MP1 buffer (2 ml g^{-1} wet weight of 0.1 M Tris base and 10 mM dithiothreitol). After incubation for 10 min at 30 °C, cells were washed with 1.2 M sorbitol, resuspended in MP2 buffer (6.7 ml g^{-1} wet weight of 20 mM KPi pH 7.4, 0.6 M sorbitol and 3 mg g^{-1} wet weight of Zymolyase (Seikagaku Biobusiness)) and incubated at 30°C for 1 h. Cells were harvested at 3,000*g* for 5 min at 4 °C, resuspended in MP3 buffer (13.4 ml g^{-1} wet weight of 0.6 M sorbitol, 10 mM Tris pH 7.4, 1 mM EDTA and 1 mM PMSF) and homogenized with 2 × 10 strokes using a tight-fitting homogenizer (Sartorius Stedim Biotech). The homogenate was centrifuged two times at 3,000*g* for 5 min at 4 °C before mitochondria were isolated by centrifugation at 15,000*g* for 15 min at 4 °C. The mitochondrial pellet was resuspended in SH buffer and frozen in liquid nitrogen before storage at −80 °C.

For isolation of mitochondrial ribosomes, approximately 50 mg of mitochondria were thawed on ice and centrifuged at 10,000*g* for 10 min at 4 °C before resuspension in lysis buffer (25 mM HEPES pH 7.4, 100 mM KCl, 20 mM magnesium acetate, 1% DDM, 1 mM PMSF and 1× cOmplete protease inhibitor (Roche) in RNAse-free H_2O) and incubation on ice for 10 min. The lysate was clarified by centrifugation two times at 20,000*g* for 10 min 4 °C before being loaded on a sucrose cushion (1.2 M sucrose, 25 mM HEPES pH 7.4, 100 mM KCl, 20 mM magnesium acetate, 0.1% DDM and 2 mM DTT in RNAse-free H_2O) and centrifuged in a TLA 120.2 rotor at 75,000 rpm (245,000*g*) for 3 h at 4 °C. The mitoribosome pellet was resuspended in a grid buffer (25 mM HEPES pH 7.4, 100 mM KCl, 20 mM magnesium acetate and 0.02% DDM in RNAse-free H_2O) and clarified through centrifugation at 20,000*g* for 10 min at 4 °C. Sample was diluted to an OD_{260} of 10 corresponding to approximately 230 nM.

Data acquisition of *tuf1Δ* sample

First, 3.5 µl of sample was applied to glow-discharged (20 mA for 60 s) QuantiFoil R2/2 Cu 300-mesh grids precoated with 3-nm carbon, using a 30-s wait time and 3-s blot time at 100% humidity and 4 °C, before plunge-freezing in liquid ethane using a Vitrobot Mark IV (FEI, Thermo Fisher Scientific). Two datasets containing 26,435 and 25,922 videos were collected on a FEI Titan Krios G3 (Thermo Fisher Scientific) transmission EM instrument operating at 300 keV and equipped with a Gatan K3 direct electron detector and a GIF quantum energy filter with a slit width of 20 eV. The videos were acquired using a pixel size of 0.828 Å and a nominal magnification of ×165,000, using the software EPU, with 40 frames per video, a defocus range of −0.4 to −2.6 µm and a total electron dose of 38 e^- per $Å^2$.

Image processing of *tuf1Δ* sample

Image processing was performed using cryoSPARC version 4.3.1 (Structura Bio) (Extended Data Fig. 4) with initial preprocessing of the two datasets following a standard processing pipeline containing patch motion correction, patch contrast transfer function (CTF) estimation and curation of exposures to remove micrographs of low quality and bad CTF estimations. Particles were picked using reference-free blob picking, which was followed by particle extraction with a box size of 600 Å that was binned twice (1.64 Å per pixel). Several rounds of two-dimensional (2D) classification were performed to generate good classes for template-based particle picking. Further rounds of 2D classification were followed by ab initio three-dimensional (3D) reconstruction and heterogeneous refinement. Classes containing unaligned particles, cytosolic ribosomes and LSU only were discarded and mitoribosome monosome particles from the two datasets were merged at this stage. The merged monosome particles were subjected to another round of 2D classification, ab initio 3D reconstruction and heterogeneous refinement that resulted in a stack of 461,825 particles. This pool of particles was first subjected to homogeneous refinement followed by focused unaligned 3D classification using a mask on the mitoribosome subunit interface to look for tRNA occupancy. No class with tRNA density in the A-site was observed, which served as a good validation that this pool of mitoribosome particles were not elongating and likely stalled at initiation. Furthermore, the 3D density acquired from the homogeneous refinement showed a weak additional density at the mRNA exit channel on the SSU. The particles were, therefore, subjected to homogeneous refinement with a binary mask covering the SSU and area around the mRNA exit channel. This was followed by unaligned 3D classification using 20 classes and a focused mask around the additional density. This resulted in two classes with a visibly similar larger density, which were subsequently merged, and one class with a smaller density all located at the mRNA exit channel. The two distinct classes of particles were used for another round of unaligned 3D classification, followed by reextraction to a box size of 640 Å (0.82 Å per pixel) and global and local CTF refinement. Finally, the two classes consisting of 24,558 and 22,558 particles were subjected to local refinement, using focused masks and a Fourier shell correlation (FSC) cutoff of 0.143, which resulted in density maps with estimated resolutions of 3.8 Å and 3.7 Å, respectively.

Model building and refinement

Using AlphaFold2 (ref. 43), we predicted the structures of yeast TA proteins, known to interact with the mRNA exit channel, to systematically test whether they could be fitted into the additional densities found in our maps. For the larger additional density, we found that three TAs of the *ATP9* mRNA, namely Aep1, Aep2 and Atp25C, fit very well when comparing the overall architecture and conformations of α-helices. The initial model for each protein was first rigid-body fitted into the density map using ChimeraX version 1.6 (University of California, San Francisco) and subsequently real-space-refined using PHENIX (version 1.21-5207)[73]. Each protein subunit was then visually inspected and manually adjusted according to their densities using torsion, planar peptide, *trans* peptide and Ramachandran restraints in Coot (version 0.9.8.1)[74]. For the yeast mitochondrial ribosome, previously published structures of the SSU (PDB 8OM4) and LSU (PDB 5MRC) were used as initial models that were rigid-body fitted into the density maps and each protein and RNA subunit manually adjusted in Coot and real-space-refined using PHENIX. An extra density, corresponding to the *ATP9* mRNA, was visibly bound to the TA protein complex and extended through the mRNA channel into the tRNA-binding sites

where it interacted with a tRNA in the E-site. An RNA backbone consisting of poly(U) (U–A in double-stranded regions) was modeled in Coot and real-space-refined using secondary structure restraints in PHENIX into this fractured density for visualization purposes. A tRNA structure (from PDB 5MRC) in the E-site was used as an initial model and its nucleotides were modified in Coot according to the nucleotide sequence of the yeast initiator fMet-tRNA. The full structure containing the mitoribosomal LSU and SSU, fMet-tRNA, mRNA and an Aep1–Aep2–Atp25C complex was subsequently real-space-refined and validated in PHENIX using a composite map, generated in ChimeraX (vop maximum command) using the consensus map and locally refined maps. The second class visibly contained a single protein density, with PPR motifs, bound at the MCE in a similar position to Aep2. We found that the predicted structure for the *ATP8* TA Aep3 fit very well into this map, which also contained partial density for double-stranded and single-stranded mRNA extending into the ribosome. A model containing Aep3 and mRNA bound to the mitoribosome was subsequently rigid-body fitted, manually adjusted and refined in the same way as the *ATP9* TA complex. Two regions predicted to consist of long flexible loops ranging encompassing residues 33–52 and 531–558 were removed because of a lack of clear density in the map.

Isolation of Aep2–ribosome complexes for cryo-EM

First, 6 l of yeast culture in YPGal pH 5.0 was grown at 30 °C until an OD_{600} between 1 and 1.5 was reached. The culture was separated into 2,000-ml aliquots in three 4-l flasks. Then, 650 g of crushed MilliQ Ice cubes were added to each flask. The flasks were quickly swirled and placed on ice. Next, 58 ml of 37% formaldehyde was added to each snap-chilled culture. Crosslinking proceeded for 1 h on ice and the flasks were swirled every 15 min to mix. Then, 142 ml of 2.5 M glycine was added to each culture to quench the crosslinking. The culture was pelleted by centrifugation for 10 min at 3,000 rpm (1,744*g*) at 4 °C. The pellet was then washed in MilliQ water twice and weighed.

The cell pellet was then resuspended with prewarmed DTT buffer (100 mM Trizma base and 10 mM DTT) at 2 ml g^{-1} wet weight. The resuspended cells were then transferred to a 250-ml flask and incubated at 30 °C for 20 min with shaking at 80 rpm. The cells were pelleted at 3,000*g* for 5 min and resuspended in 7 ml g^{-1} Zymolyase buffer (1.2 M sorbitol and 20 mM potassium phosphate, pH 7.4) containing 3 mg of Zymolyase 20T (MP Biomedicals) per gram of wet weight. The resuspended cells were then transferred to a flask and shaken at 80 rpm at 30 °C for 1 h. The cells were then pelleted for 5 min at 3,000*g* and washed with fresh Zymolyase buffer without Zymolyase 20T. The cells were then resuspended in 6.5 ml g^{-1} ice-cold homogenization buffer (0.6 M sorbitol, 10 mM Tris-HCl pH 7.4 and 1× protease inhibitor cocktail EDTA-free) and homogenized using a glass Dounce homogenizer for 20 strokes on ice. Following homogenization, the lysate was diluted with an equal volume of cold homogenization buffer. Cell debris and nuclei were then pelleted by spinning the lysate at 1,500*g* for 5 min at 4 °C. The supernatant was then further clarified by an additional spin at 3,000*g* for 10 min. Using a SW41-Ti rotor, mitochondria were pelleted from the supernatant at 12,000*g* for 15 min. The mitochondrial pellet was then resuspended in 5 ml of lysis buffer without lauryl maltoside (50 mM HEPES pH 7.5, 50 mM NH_4Cl, 10 mM $MgCl_2$, 1.5× protease inhibitor cocktail EDTA-free and 1% lauryl maltoside). The resuspended mitochondria were then flash-frozen in liquid nitrogen and stored at −80 °C.

Six 10–50% sucrose gradients were prepared using 10% (50 mM HEPES pH 7.5, 50 mM NH_4Cl, 10 mM $MgCl_2$, 1× protease inhibitor cocktail EDTA-free and 10% sucrose) and 50% (50 mM HEPES pH 7.5, 50 mM NH_4Cl, 10 mM $MgCl_2$, 1× complete protease inhibitor cocktail EDTA-free (Roche) and 50% sucrose) sucrose solutions using the Biocomp Gradient Master using the 10–50% SW41 14s preset program. The isolated mitochondria were thawed in a water bath at room temperature, inverted to mix and placed on ice. Next, 25 µl of SUPERase-In RNase inhibitor and 1 ml of 5% lauryl maltoside were added to the isolated mitochondria. The mitochondria were then pipetted up and down with a 5-ml pipette tip and incubated on ice for 1 h to lyse the mitochondria. The mitochondrial lysate was then clarified by centrifuging for 20 min at 20,000*g* at 4 °C. Then, 750 µl of clarified lysate was added slowly to the top of each 10–50% sucrose gradient. The gradients were centrifuged for 3 h at 40,000 rpm (274,000*g*) at 4 °C in an SW41-TI rotor. The gradients were fractionated into 13 fractions of 850 µl and a Triax flow cell was used to measure the OD_{260} for RNA abundance within each fraction. The monosome fractions from each sucrose gradient were pooled and 18 µl of 5% lauryl maltoside, 50 µl of SUPERase-In RNase inhibitor and 210 µl of 50× complete protease inhibitor cocktail EDTA-free were added to the pooled fractions.

The pooled monosome fractions were then incubated overnight at 4 °C with end-over-end rotation with 50 µl of packed anti-FLAG M2 affinity resin (Millipore-Sigma). The anti-FLAG affinity resin was then washed three times with 1 ml of mitoribosome wash buffer with lauryl maltoside (50 mM HEPES pH 7.5, 50 mM NH_4Cl, 10 mM $MgCl_2$ and 0.1% lauryl maltoside). After the last wash, the FLAG resin was resuspended with 1 ml of elution buffer (50 mM HEPES pH 7.5, 50 mM NH_4Cl, 10 mM $MgCl_2$ and 0.02% lauryl maltoside) and transferred to a clean 1.5-ml tube. The Aep2–FLAG ribosome complexes were then eluted from the resin with 600 µl of elution buffer with 200 µg ml^{-1} 3×FLAG peptide for 1 h at 4 °C with end-over-end rotation. A second elution was carried out with 600 µl of elution buffer with FLAG peptide and the two elutions were pooled together and concentrated using a 500-µl 100-kDa PES protein concentrator (Pierce).

Data acquisition of Aep2-bound mitoribosome sample

For the Aep2-bound mitoribosomes, 3.5 µl of the affinity-purified mitoribosome sample was applied to glow-discharged R2/2 copper 400-mesh grids (Quantifoil) covered with a 5-nm layer of continuous carbon and plunge-frozen in liquid ethane using a Vitrobot Mark IV (Thermo Fisher Scientific) that was set at 4 °C and 100% humidity with a 10-s wait time, 3-s blot time and +6 blot force. The grids were first screened using a 200-kV Talos Arctica (Thermo Fisher Scientific). The final dataset was collected using a 300-kV Titan Krios (Thermo Fisher Scientific), equipped with a Falcon 4i camera (Thermo Fisher Scientific) and Selectris energy filter of 10-eV slit width, in counting mode at a nominal magnification of ×105,000, corresponding to a calibrated pixel size of 1.19 Å. A total of 15,728 electron-event representation video frames were acquired with a total exposure time of 6 s, corresponding to a total dose of 48.5 e^- per $Å^2$. The defocus values were set from −0.8 to −2.0 µm. Semiautomated data collection was performed with EPU (Thermo Fisher Scientific).

Cryo-EM data processing of Aep2-bound mitoribosome

Data processing of the Aep2-bound mitoribosomes (Extended Data Fig. 9) was performed using both RELION (version 4.0.1)[75] and with cryoSPARC (version 4.3.1)[76]. The video frames were motion-corrected using RELION's own implementation and CTF estimation was performed using CTFFind (version 4.1)[77]. A total of 874,238 particles were picked using automated particle picking in RELION (version 4.0.1) and extracted with a particle box size of 420 pixels, rescaled to 210 pixels with a size of 2.38 Å per pixel. Multiple rounds of 2D classification were performed to get rid of nonribosomal particles. The selected particles from the best 2D classes were used for 3D classification and subsequent 3D refinement. The duplicated particles were removed from the refined particles, particles were reextracted to a full pixel size of 1.19 Å per pixel and imported into cryoSPARC (version 4.3.1) for further processing.

The imported 136,281 particles were subjected to homogeneous refinement in cryoSPARC (version 4.3.1) and they were further taken for particle signal subtraction using masks generated by using either SSU or LSU from prior processing steps from RELION (version 4.0.1). For both LSU and SSU, the signal-subtracted particles were subjected to 3D classification with no alignments and the best classes were further

subjected to homogeneous refinement followed by global and local CTF refinements, resulting in density maps with estimated resolutions of 2.9 Å for LSU and 3.6 Å for SSU (FSC cutoff = 0.143). To further obtain a better TA (Aep1–Aep2–Atp25C complex) density, particles from the refined SSU were taken and signal-subtracted using a mask made to keep only the TA density. After the signal subtraction, 3D classification with no alignment followed by local refinement was performed resulting in density map with estimated resolution of 4.4 Å (FSC cutoff = 0.143). Furthermore, the TA map was fitted onto SSU map in ChimeraX and a composite map was generated using ChimeraX (vop maximum command) by resampling the TA map on the coordinates of the SSU map.

co-IP of Aep1 and Aep2 from whole-cell lysate

Yeast cells were grown to an OD_{600} between 0.6 and 0.8 and harvested by rapid filtration and flash-freezing in liquid nitrogen. The frozen cell pellet was then mixed with 4 ml of frozen crosslinking lysis buffer and mechanical lysis of the cells was performed as described for sel-mitoRP. The frozen lysate was thawed at room temperature and precleared by centrifugation at 3,000 rpm (1,744*g*) for 5 min, followed by another preclearing step of 20,000*g* for 15 min. Each sample was incubated overnight with 40 µl of packed anti-FLAG agarose resin with end-over-end rotation at 4 °C. The flowthrough was removed and the beads were washed three times with 1 ml of mitoribosome wash buffer. The proteins were eluted with 200 µg ml^{-1} 3×FLAG peptide for 1 h at 4 °C.

Reporting summary

Further information on research design is available in the Nature Portfolio Reporting Summary linked to this article.

Data availability

Raw and processed sequencing data generated in this study were deposited to the Gene Expression Omnibus under accession number GSE282943. Mitoribosome footprints without crosslinking (steady-state glycerol growth) are available under accession number GSE74454. Cryo-EM densities were deposited to the EM Data Bank under accession codes EMD-52281 (Aep1–Aep2–Atp25C, composite), EMD-52235 (Aep1–Aep2–Atp25C, consensus), EMD-52270 (Aep1–Aep2–Atp25C, TA), EMD-52252 (Aep1–Aep2–Atp25C, SSU body), EMD-52256 (Aep1–Aep2–Atp25C, SSU head), EMD-52257 (Aep1–Aep2–Atp25C, LSU), EMD-52283 (Aep3, composite), EMD-52277 (Aep3, consensus), EMD-52276 (Aep3, TA), EMD-52278 (Aep3, SSU body), EMD-52279 (Aep3, SSU head), EMD-52280 (Aep3, LSU), EMD-48387 (Aep2–FLAG affinity-purified, TA), EMD-48388 (Aep2–FLAG affinity-purified, SSU), EMD-48390 (Aep2–FLAG affinity-purified, LSU) and EMD-48700 (Aep2–FLAG affinity-purified, composite map of SSU and Aep1–Aep2–Atp25C complex). Atomic models were deposited to the Protein Data Bank under accession codes 9HLZ (Aep1–Aep2–Atp25C, composite) and 9HM0 (Aep3, composite). Other models used in this study were also obtained from the PDB under accession codes 5MRC (yeast mitoribosome) and 8OM4 (yeast mitoribosome, SSU). Source data are provided with this paper.

Code availability

Scripts used to analyze sel-mitoRP are available from GitHub (https://github.com/churchmanlab/Yeast_selective_mitoRP).

References

61. Gietz, R. D. & Schiestl, R. H. Large-scale high-efficiency yeast transformation using the LiAc/SS carrier DNA/PEG method. *Nat. Protoc.* **2**, 38–41 (2007).
62. Alani, E., Cao, L. & Kleckner, N. A method for gene disruption that allows repeated use of URA3 selection in the construction of multiply disrupted yeast strains. *Genetics* **116**, 541–545 (1987).
63. Moqtaderi, Z. & Struhl, K. Expanding the repertoire of plasmids for PCR-mediated epitope tagging in yeast. *Yeast* **25**, 287–292 (2008).
64. Götzke, H. et al. The ALFA-tag is a highly versatile tool for nanobody-based bioscience applications. *Nat. Commun.* **10**, 4403 (2019).
65. Gruschke, S. et al. Proteins at the polypeptide tunnel exit of the yeast mitochondrial ribosome. *J. Biol. Chem.* **285**, 19022–19028 (2010).
66. Prestele, M., Vogel, F., Reichert, A. S., Herrmann, J. M. & Ott, M. Mrpl36 is important for generation of assembly competent proteins during mitochondrial translation. *Mol. Biol. Cell* **20**, 2615–2625 (2009).
67. Couvillion, M. T. & Churchman, L. S. Mitochondrial ribosome (mitoribosome) profiling for monitoring mitochondrial translation in vivo. *Curr. Protoc. Mol. Biol.* **119**, 4.28.1–4.28.25 (2017).
68. Martin, M. Cutadapt removes adapter sequences from high-throughput sequencing reads. *EMBnet J.* **17**, 10 (2011).
69. Langmead, B., Trapnell, C., Pop, M. & Salzberg, S. L. Ultrafast and memory-efficient alignment of short DNA sequences to the human genome. *Genome Biol.* **10**, R25 (2009).
70. Dobin, A. et al. STAR: ultrafast universal RNA-seq aligner. *Bioinformatics* **29**, 15–21 (2013).
71. Carlström, A., Rzepka, M. & Ott, M. The analysis of yeast mitochondrial translation. *Methods Mol. Biol.* **2192**, 227–242 (2021).
72. Gruschke, S. et al. Cbp3–Cbp6 interacts with the yeast mitochondrial ribosomal tunnel exit and promotes cytochrome b synthesis and assembly. *J. Cell Biol.* **193**, 1101–1114 (2011).
73. Liebschner, D. et al. Macromolecular structure determination using X-rays, neutrons and electrons: recent developments in PHENIX. *Acta Crystallogr. D* **75**, 861–877 (2019).
74. Lohkamp, B., Scott, W. G. & Cowtan, K. Features and development of Coot. *Acta Crystallogr. D* **66**, 486–501 (2010).
75. Scheres, S. H. W. RELION: implementation of a Bayesian approach to cryo-EM structure determination. *J. Struct. Biol.* **180**, 519–530 (2012).
76. Punjani, A., Rubinstein, J. L., Fleet, D. J. & Brubaker, M. A. cryoSPARC: algorithms for rapid unsupervised cryo-EM structure determination. *Nat. Methods* **14**, 290–296 (2017).
77. Rohou, A. & Grigorieff, N. CTFFIND4: fast and accurate defocus estimation from electron micrographs. *J. Struct. Biol.* **192**, 216–221 (2015).

Acknowledgements

We thank A. Amunts and Y. Zgadzay for help and advice on attempts to obtain the Aep2 mitoribosome structure. We thank C. Nuessmeier and G. Prakash for careful review of the manuscript. We thank T. Fox and members of the L.S.C. and F. M. Winston (Harvard Medical School) labs for advice and discussions. We acknowledge the Harvard Center for Cryo-EM for cryo-EM data collection and SBGrid for support of data processing. The cryo-EM data of *tuf1*Δ mitoribosome complexes were collected at the Swedish national cryo-EM facility in Solna funded by the Knut and Alice Wallenberg Foundation, Erling Persson and Kempe Foundations. This work was supported by National Institutes of Health (R01-GM123002, to L.S.C.), the Swedish Research Council (2018-03694 and 2021-05545, to M.O.), the Knut and Alice Wallenberg foundation (2017.009 and 2019.0319, to M.O.) and the Packard Foundation (to S.S.). D.S. is a European Molecular Biology Organization postdoctoral fellow. S.S. is an investigator with the Howard Hughes Medical Institute. The funders had no role in study design, data collection and analysis, decision to publish or preparation of the manuscript.

Author contributions

J.B.B. generated FLAG-tagged yeast strains for sel-mitoRP and performed the sel-mitoRP. J.B.B. and M.T.C. analyzed the sel-mitoRP

sequencing results. B.W. and J.B.B. performed the co-IP of Aep1 and Aep2 from whole-cell lysate. J.B.B. purified the Aep2-bound mitoribosomes for cryo-EM. J.G. and D.S. made the cryo-EM grids for the Aep2 affinity-purified mitoribosomes, collected the data and determined the structure. A.C. generated the *tuf1* deletion strain, purified the TA–mitoribosome complexes from this strain, made the cryo-EM grids and performed the cryo-EM screening, data collection, structure determination and model building with the help of U.R. J.B.B., A.C. and D.S. prepared the figures and a first draft of the manuscript. S.S., M.O. and L.S.C. supervised the project, interpreted the data and wrote the paper. All authors contributed toward the final version of the paper.

Funding

Open access funding provided by University of Gothenburg.

Competing interests

The authors declare no competing interests.

Additional information

Extended data is available for this paper at https://doi.org/10.1038/s41594-025-01726-y.

Supplementary information The online version contains supplementary material available at https://doi.org/10.1038/s41594-025-01726-y.

Correspondence and requests for materials should be addressed to Sichen Shao, Martin Ott or L. Stirling Churchman.

Peer review information *Nature Structural & Molecular Biology* thanks Rajendra Agrawal and the other, anonymous, reviewer(s) for their contribution to the peer review of this work. Primary Handling Editor: Sara Osman, in collaboration with the *Nature Structural & Molecular Biology* team.

https://doi.org/10.1038/s41594-025-01726-y

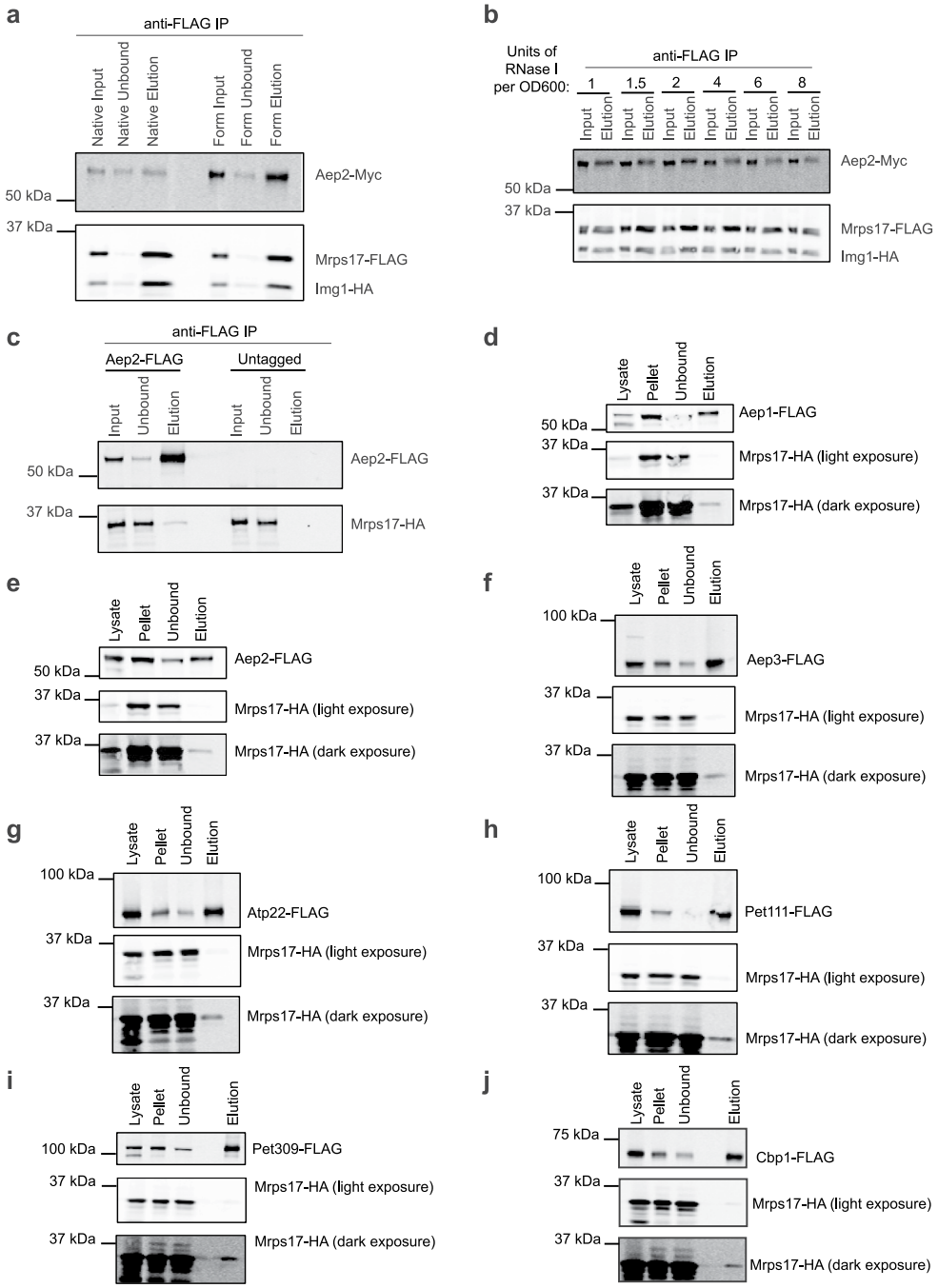

Extended Data Fig. 1 | Optimization of TA co-purification with the mitoribosome. a, Western blot of Myc-tagged Aep2 co-purified with a 3X-FLAG-tagged mitoribosome from the monosome fraction of a 10-50% continuous sucrose gradient (Input). The co-IP was performed from yeast cells treated with (Form) or without (Native) formaldehyde crosslinking. This is a representative western blot taken from two biological replicates. **b**, Crosslinked yeast lysates were pretreated with increasing amounts of RNase I prior to affinity purification of Mrps17-FLAG mitoribosomes from the monosome fraction of a 10-50% sucrose gradient (Input). Continued interaction of Aep2-Myc with the mitoribosome was tested at each indicated concentration of RNase I. This is a representative blot from at least two biological replicates. **c**, FLAG affinity purification from the monosome fraction of a 10-50% sucrose gradient was carried out for an Aep2-FLAG strain and untagged control demonstrating specific co-purification of the mitoribosome only when Aep2 is tagged. This is a representative western blot from two biological replicates. **d-j**, Western blots from the sel-mitoRP co-IP of the given FLAG-tagged TA and the HA-tagged mitoribosome. The blots were imaged on a LICOR machine and low contrast (low exposure) and high contrast (high exposure) images are shown. Lysate refers to the RNase treated lysate prior to its pelleting through a sucrose cushion. Pellet refers to the protein material recovered from the resuspended ribosome pellet. Unbound is the protein that was not bound to the anti-FLAG agarose resin. Elution is the material that was eluted off the anti-FLAG resin with 3X-FLAG peptide. All western blots shown are representative blots from at least two biological replicates.

https://doi.org/10.1038/s41594-025-01726-y

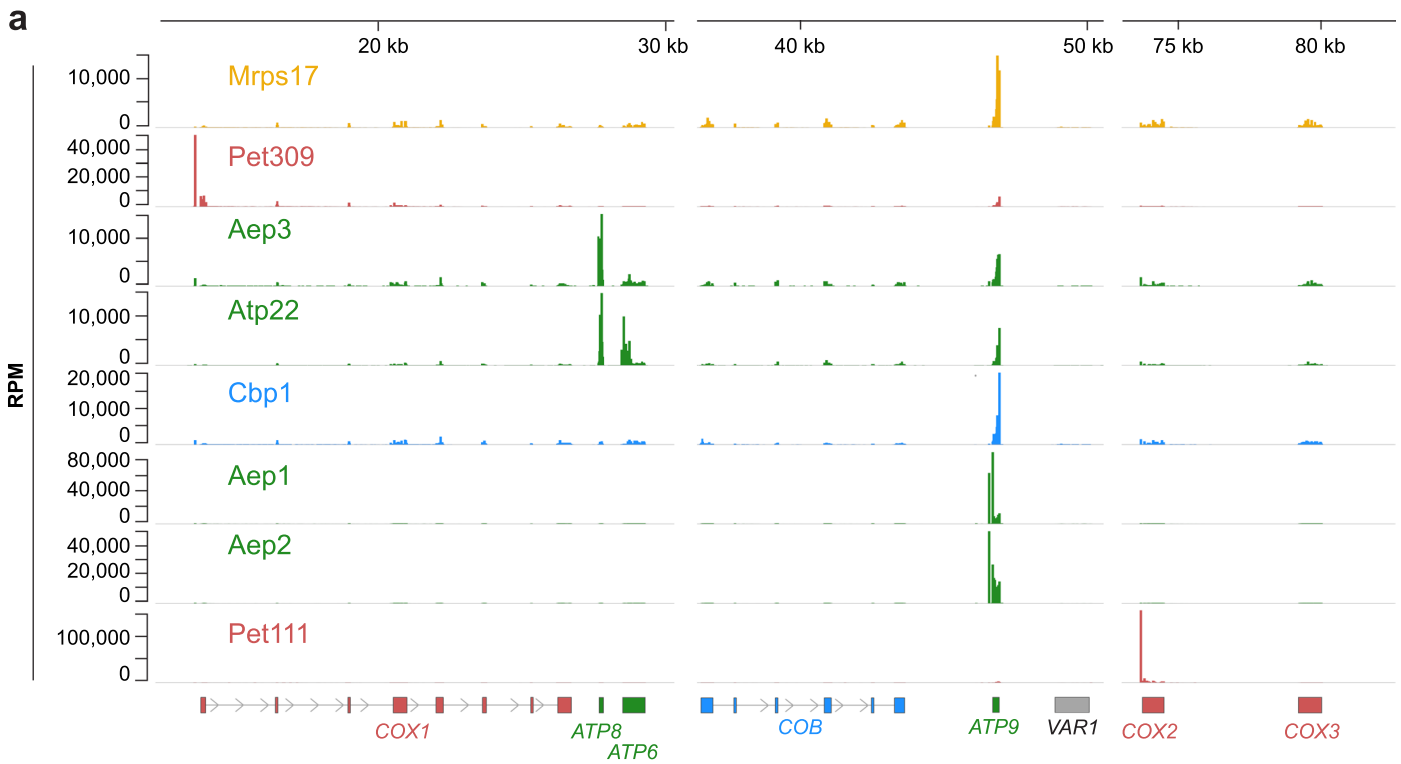

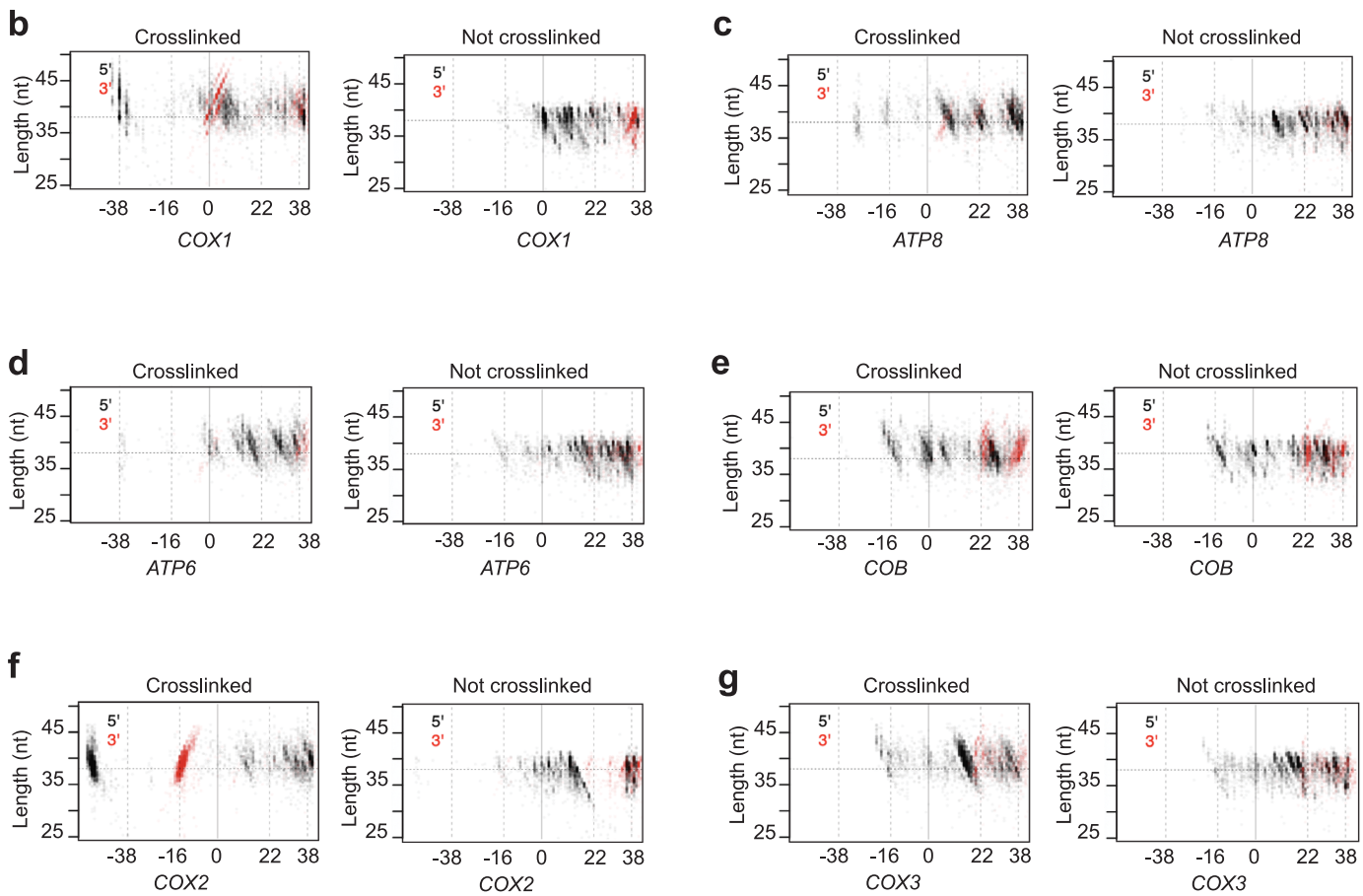

Extended Data Fig. 2 | Sel-mitoRP data without Mrps17 normalization and V-plots showing extended 5′ end protection with crosslinking. a, Inferred A-sites for Mrps17 and all sel-mitoRP datasets normalized to total reads mapping to the mitochondrial genome (RPM). RPM = reads per million mapped reads. **b-g**, Plots comparing total mitoribosome profiling either with or without crosslinking for the given transcript. 5′ ends of RNA footprints are plotted in black and 3′ ends are plotted in red. The horizontal dashed line indicates a standard initiating mitoribosome footprint size of 38 nucleotides. For all transcripts except for *COB* and *COX3*, a clear extension to the 5′ end of the initiating mitoribosome can be visualized upon the addition of formaldehyde crosslinking. All data consist of combined reads from at least two biological replicates.

https://doi.org/10.1038/s41594-025-01726-y

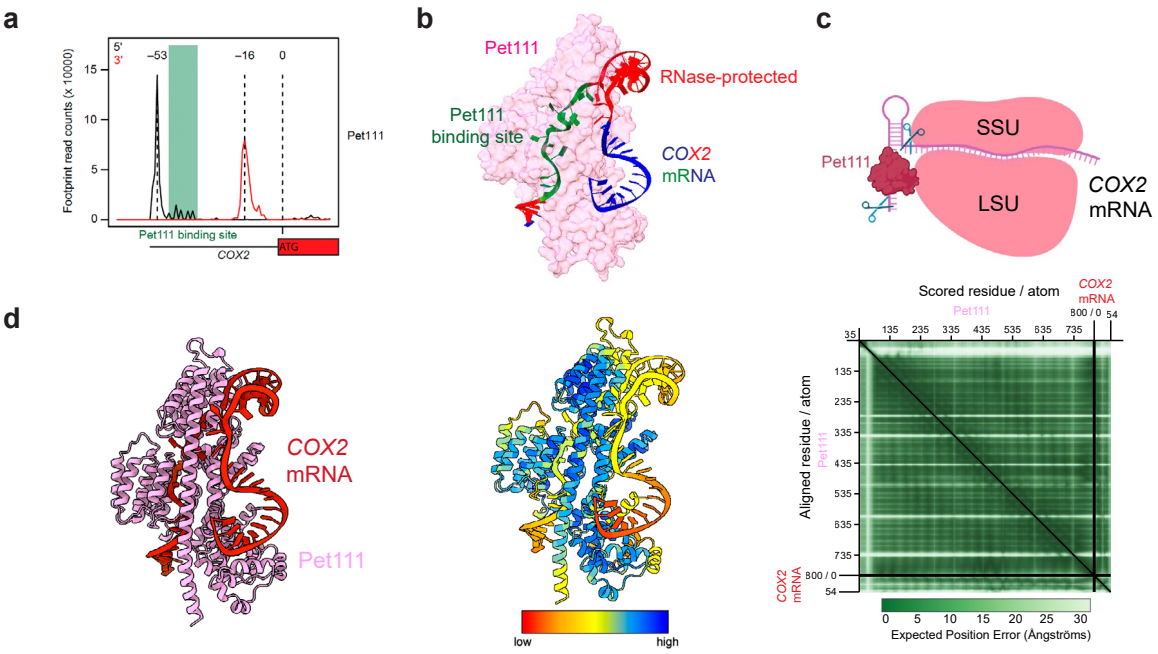

Pet111-*COX2* mRNA AF3 model colored based on protein subunit and RNA

Pet111-*COX2* mRNA AF3 model colored based on pLDDT score

PAE plot for Pet111-*COX2* mRNA AF3 model

Extended Data Fig. 3 | Structure prediction of Pet111 bound to the *COX2* 5′ UTR. a, The read counts for the 5′ and 3′ ends of Pet111 sel-mitoRP footprints are plotted in relation to the Pet111 binding site in the 5′ UTR of *COX2*. 5′ ends are plotted in black and 3′ ends are plotted in red. Data shown consist of combined reads from two biological replicates. **b**, The AlphaFold3 structural prediction of Pet111 (magenta) bound to its target site in the *COX2* 5′ UTR. The Pet111 binding site is highlighted in green and the RNase-protected region (red) indicates the bounds of the 5′ and 3′ end peaks that surround the Pet111 binding site in panel a. **c**, Model of Pet111 bound to *COX2* upstream of the predicted stem loop structure with Rnase I (scissors) cutting the RNA upstream of Pet111 and downstream of the stem loop. **d**, Alphafold3 prediction of Pet111 (magenta) bound to the *COX2* 5′ UTR (red), color-coded based on protein subunit and mRNA (left panel) and pLDDT (predicted local distance difference test) score (middle panel). The PAE (predicted aligned error) plot of the AF3 model is shown in the right panel. Panel **c** created with BioRender.com.

https://doi.org/10.1038/s41594-025-01726-y

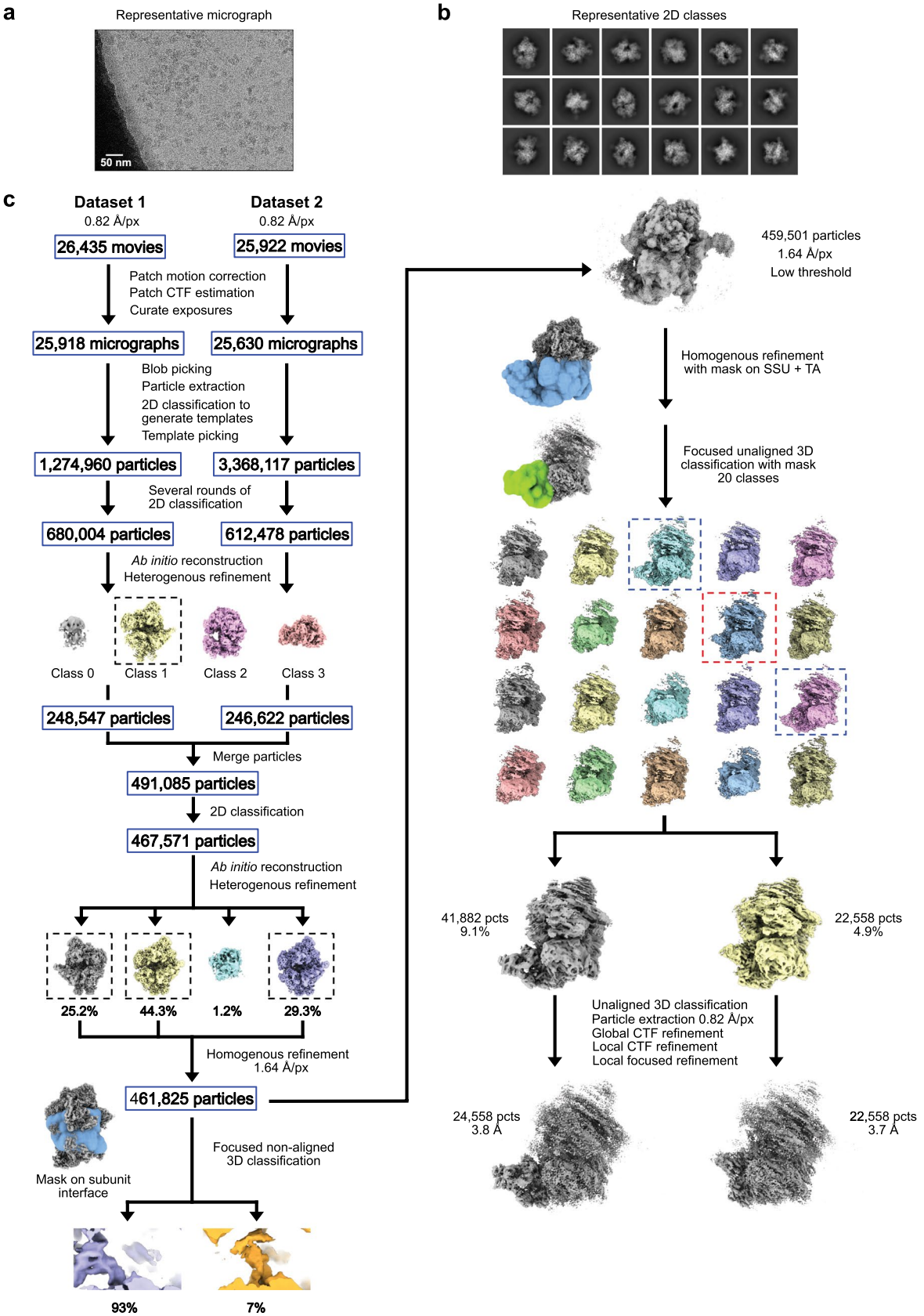

Extended Data Fig. 4 | See next page for caption.

https://doi.org/10.1038/s41594-025-01726-y

Extended Data Fig. 4 | Cryo-EM processing workflow for *tuf1Δ* mitoribosomes. **a**, Representative micrograph of mitoribosome particles from the *tuf1Δ* sample. This experiment was repeated twice and yielded similar results. **b**, Representative 2D class averages of mitoribosome particles from the *tuf1Δ* sample. **c**, Schematic depicting the overall cryo-EM data processing workflow for the stalled post-initiating mitoribosomes from the *tuf1Δ* sample. Two data sets collected from the same grid were subjected to similar pre-processing in cryoSPARC v4.3.1 containing Patch motion correction, Patch CTF estimation, particle picking, 2D classification, *ab-initio* reconstruction and heterogenous refinement before merging of particles. Merged mitoribosome monosome particles were subsequently subjected to homogenous refinement followed by focused non-aligned 3D classification with a binary mask covering the subunit interface (to investigate tRNA occupancy) or the mitoribosomal SSU and the mRNA exit channel. The latter resulted in two major classes with additional densities located at the mRNA exit channel. Local refinement of the two classes resulted in overall estimated resolutions of 3.8 Å and 3.7 Å, respectively.

https://doi.org/10.1038/s41594-025-01726-y

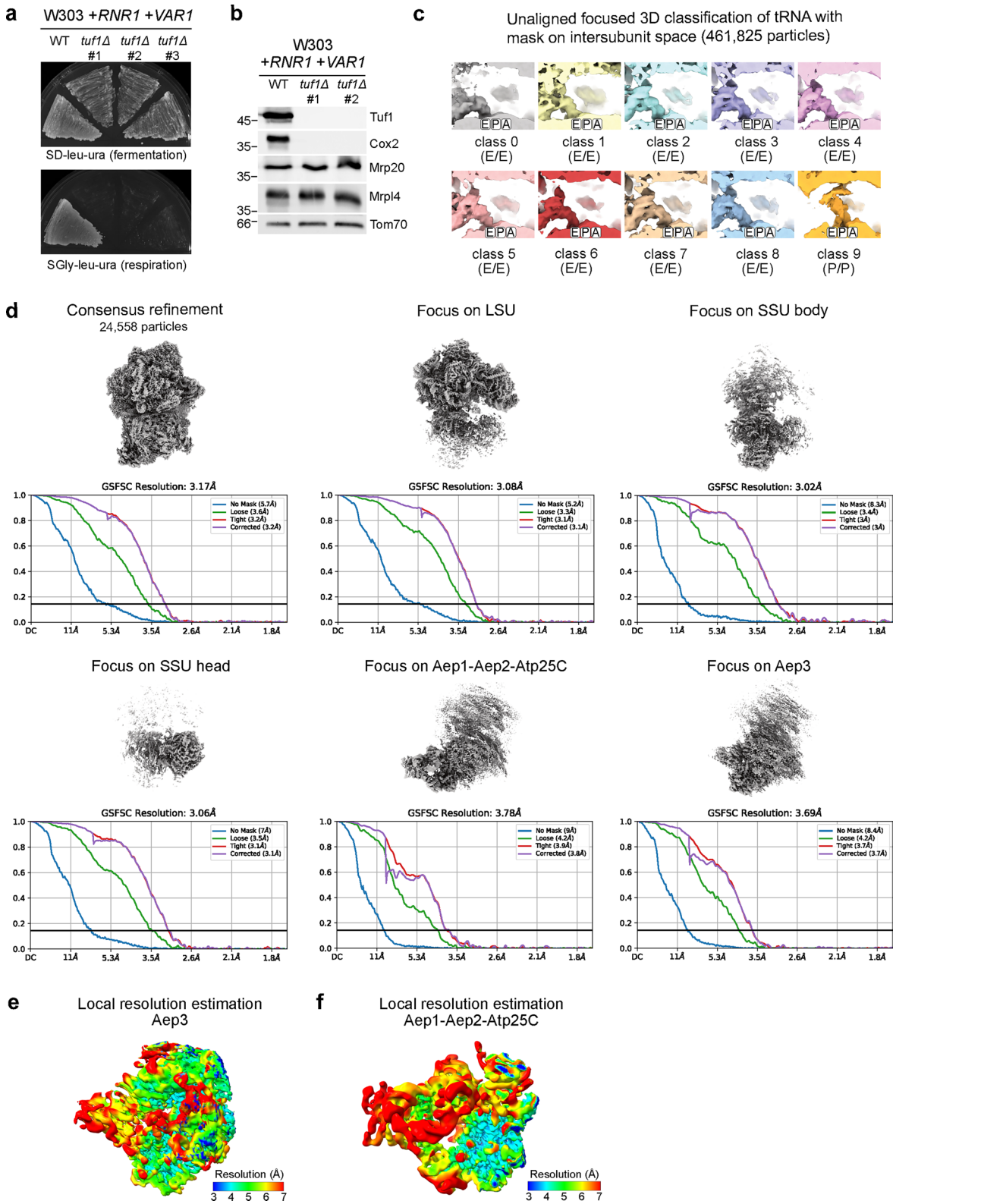

Extended Data Fig. 5 | Strain characterization, tRNA occupancy, refined maps and local resolution estimations for the *tuf1Δ* mitoribosomes. **a**, Growth test of wild-type (W303 + *RNR1* + VAR1) and *tuf1Δ* (clones #1-3) cells on fermentative (SD-leu-ura) and respiratory (SGly-leu-ura) media. This experiment was repeated twice with similar results. **b**, Steady-state protein levels in wild-type (W303 + *RNR1* + VAR1) and *tuf1Δ* (clones #1-2) cells. Absence of Tuf1 led to abolished synthesis of Cox2 but with an intact mitoribosome as evidenced by stable levels of Mrp20 and Mrpl4. Tom70 was used as a loading control. This experiment was repeated twice with similar results. **c**, Visualization of 10 classes after focused 3D classification using a binary mask on the subunit interface. Classes 0 to 8 show a tRNA density in the E-site, interacting with the L1 stalk of the LSU, while solely class 9 showed a density occupying the P-site. **d**, Density map of the consensus refinement for *ATP9* initiating mitoribosomes using 24,558 particles and locally refined density maps of the LSU, SSU body, SSU head, Aep1-Aep2-Atp25C and Aep3 with their respective gold-standard Fourier shell correlation (GSFSC) curves with a cut-off at 0.143. **e**,**f**, Local resolution estimations of the Aep3 and Aep1-Aep2-Atp25C focused refined maps, with local resolution estimates ranging between 4 and 7 Å for the protein subunits and 6 Å and above for the mRNA densities.

https://doi.org/10.1038/s41594-025-01726-y

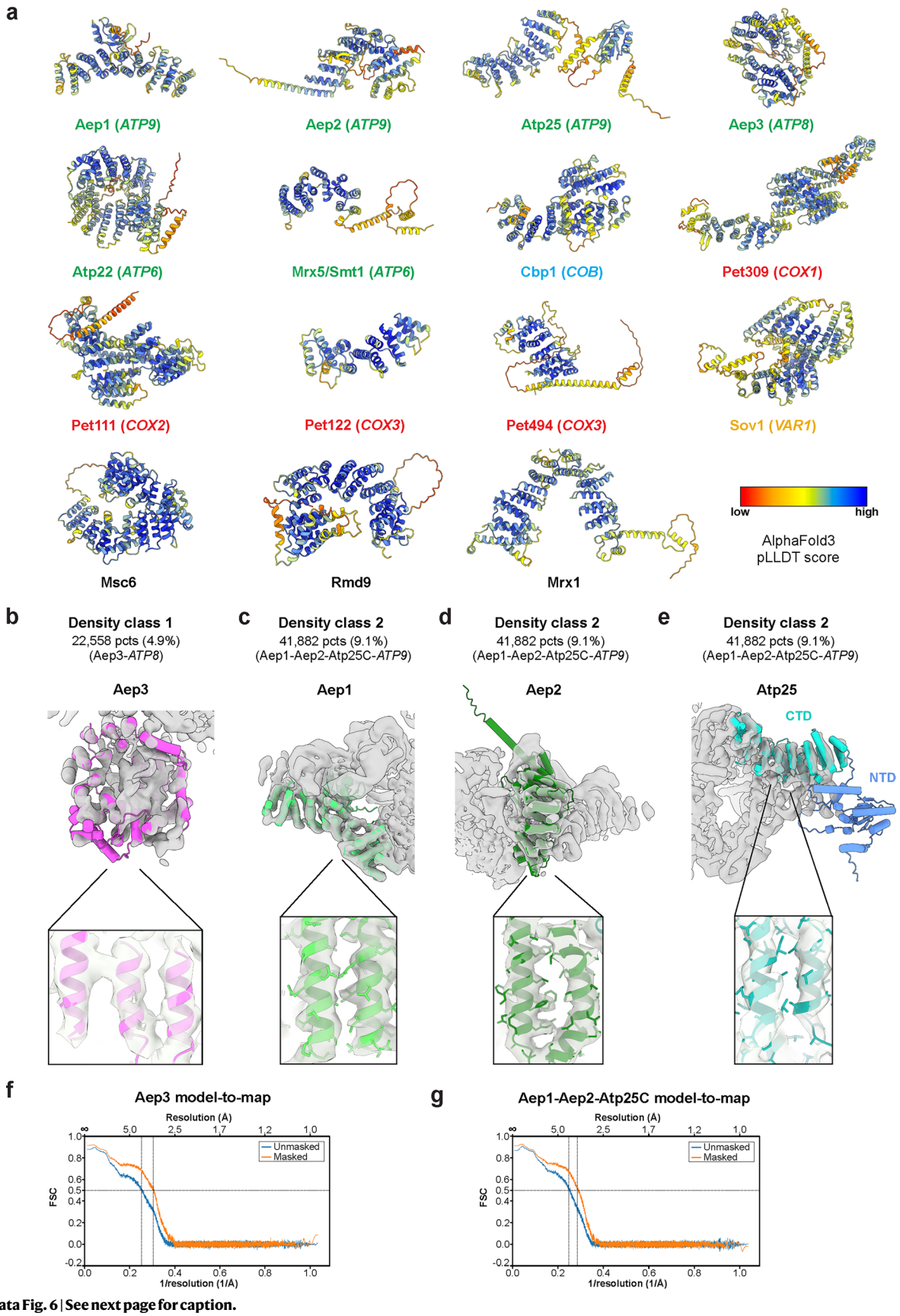

Extended Data Fig. 6 | See next page for caption.

https://doi.org/10.1038/s41594-025-01726-y

Extended Data Fig. 6 | AlphaFold3 models of mitochondrial PPR motif proteins and the fit of Aep3, Aep1, Aep2 and Atp25 to their respective density. **a**, AlphaFold3 predicted models of TAs in *S. cerevisiae* mitochondria with known or predicted PPR domains together with the three more uncharacterized PPR proteins Msc6, Rmd9 and Mrx1, color- coded based on pLDDT confidence score. TAs involved in synthesis of subunits of the ATP synthase, complex III, complex IV and the mitoribosome are labelled in green, blue, red and yellow, respectively. Individual rigid-body fitting of all the predicted structures showed that Aep3 (**b**) fit the best into the smaller additional density of the first cryo-EM map shown in Fig. 3, while Aep1 (**c**), Aep2 (**d**) and Atp25C (**e**) fit very well into the second cryo-EM map with larger additional density shown in Fig. 3. **f**, Model-to-map FSC curve for the Aep3-mitoribosome complex. **g**, Model-to-map FSC curve for the Aep1-Aep2-Atp25C-mitoribosome complex.

https://doi.org/10.1038/s41594-025-01726-y

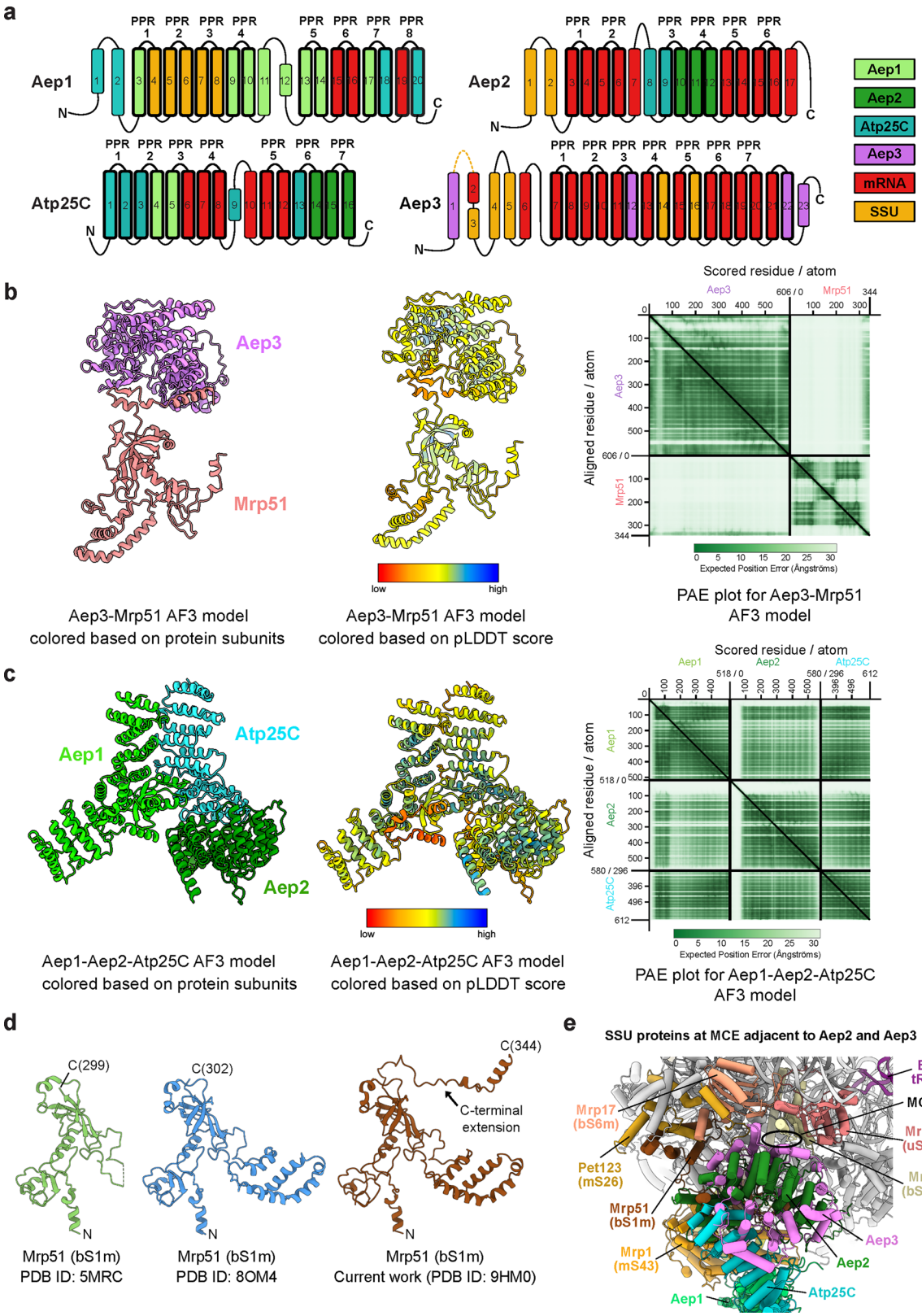

Extended Data Fig. 7 | See next page for caption.

https://doi.org/10.1038/s41594-025-01726-y

Extended Data Fig. 7 | AlphaFold3 modeling of Aep3- Mrp51 complex and ATP9 TA complex. a, Linear diagrams of Aep1 (light green), Aep2 (forest green), Atp25C (cyan) and Aep3 (lavender) demonstrating which PPR motifs and alpha-helices are engaged with mRNA (red), the SSU (yellow) and the other TAs in their respective complex. Broader outline of depicted helices indicate that they are part of a PPR motif. The diagram depicts only the structural parts visible in our cryo-EM densities. The dashed line in Aep3 represents residues 33 to 52 which were not modelled in the structure. **b**, AlphaFold3-predicted model of Aep3 in complex with Mrp51 (bS1m) color-coded based on subunits (left panel) and the pLDDT confidence score (middle panel). The PAE (predicted aligned error) plot of the AF3 prediction is shown in the right panel. **c**, AlphaFold3 multimer prediction of a complex containing Aep1-Aep2-Atp25C, color-coded based on subunits (left panel) and the pLDDT confidence score (middle panel). The PAE (predicted aligned error) plot of the AF3 prediction is shown in the right panel. **d**, The SSU protein Mrp51 (bS1m) depicted as it was modelled in previously published structures with PDB ID 5MRC (green) and 8OM4 (blue), compared to the prediction and model in this current work (brown). Of note is the flexible C-terminal extension predicted to interact with Aep3. **e**, Overlay of the *ATP9* TA complex (Aep1, light green, Aep2, forest green and Atp25C, cyan) with Aep3 (lavender) on the mitoribosome (gray) showing an overlapping binding site at the MCE. Both Aep2 and Aep3 are located adjacent to SSU proteins Mrp51 (brown), Mrp21 (light olive), Mrps18 (salmon), Pet123 (gold) and Mrp17 (light salmon).

https://doi.org/10.1038/s41594-025-01726-y

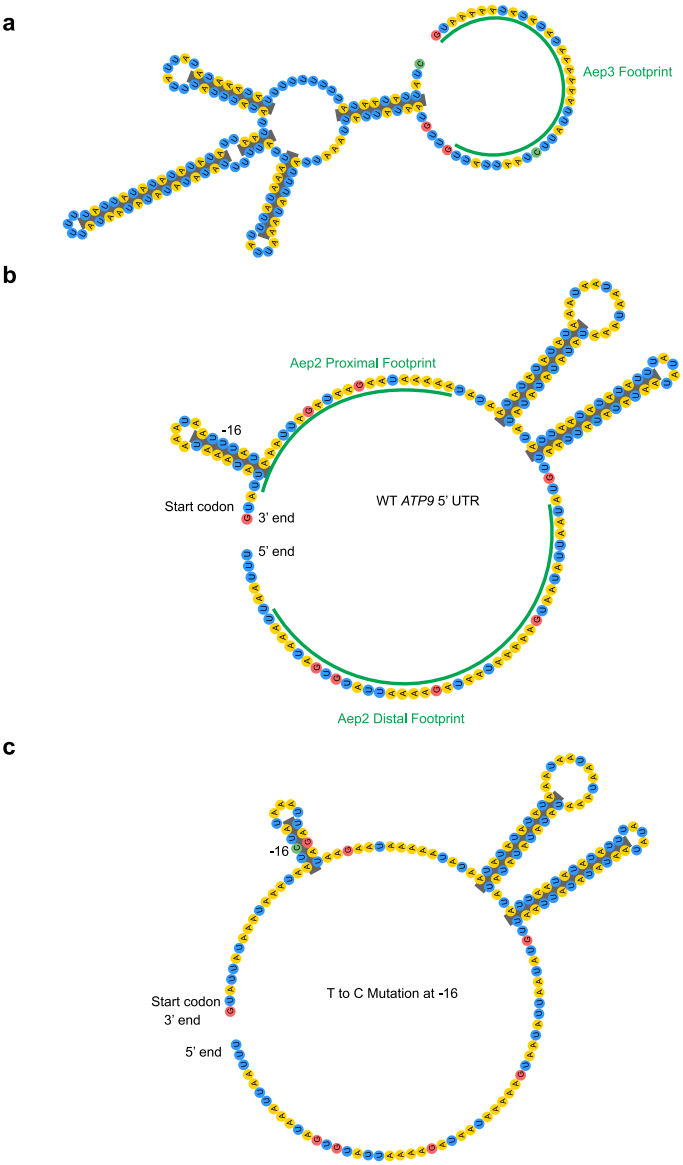

Extended Data Fig. 8 | Predicted secondary structures in the 5′ UTRs of *ATP8* and *ATP9*. a, Eternafold secondary structure prediction of the 5′ UTR of *ATP8* upstream of the Aep3-mitoribosome footprint (underlined in green). **b**, Eternafold was used to predict the secondary structure of the 5′ UTR of *ATP9* from the start codon until just upstream of the distal Aep2 sel-mitoRP footprint. Both the proximal and distal Aep2 footprints are underlined in the predicted RNA structure diagram. A stem loop is predicted to form just upstream of the start codon where we see an overlapping Aep2 footprint. Two larger stem loops are predicted to form between the two binding sites, bringing the two footprints in close proximity in three-dimensional space. **c**, A mutation known to rescue a temperature sensitive mutant of Aep2 in which a T at −16 is converted to a C was modeled in Eternafold to visualize how the secondary structure of the RNA might change. A novel stem loop is generated due to base pairing between the C at −16 and the G at −26.

https://doi.org/10.1038/s41594-025-01726-y

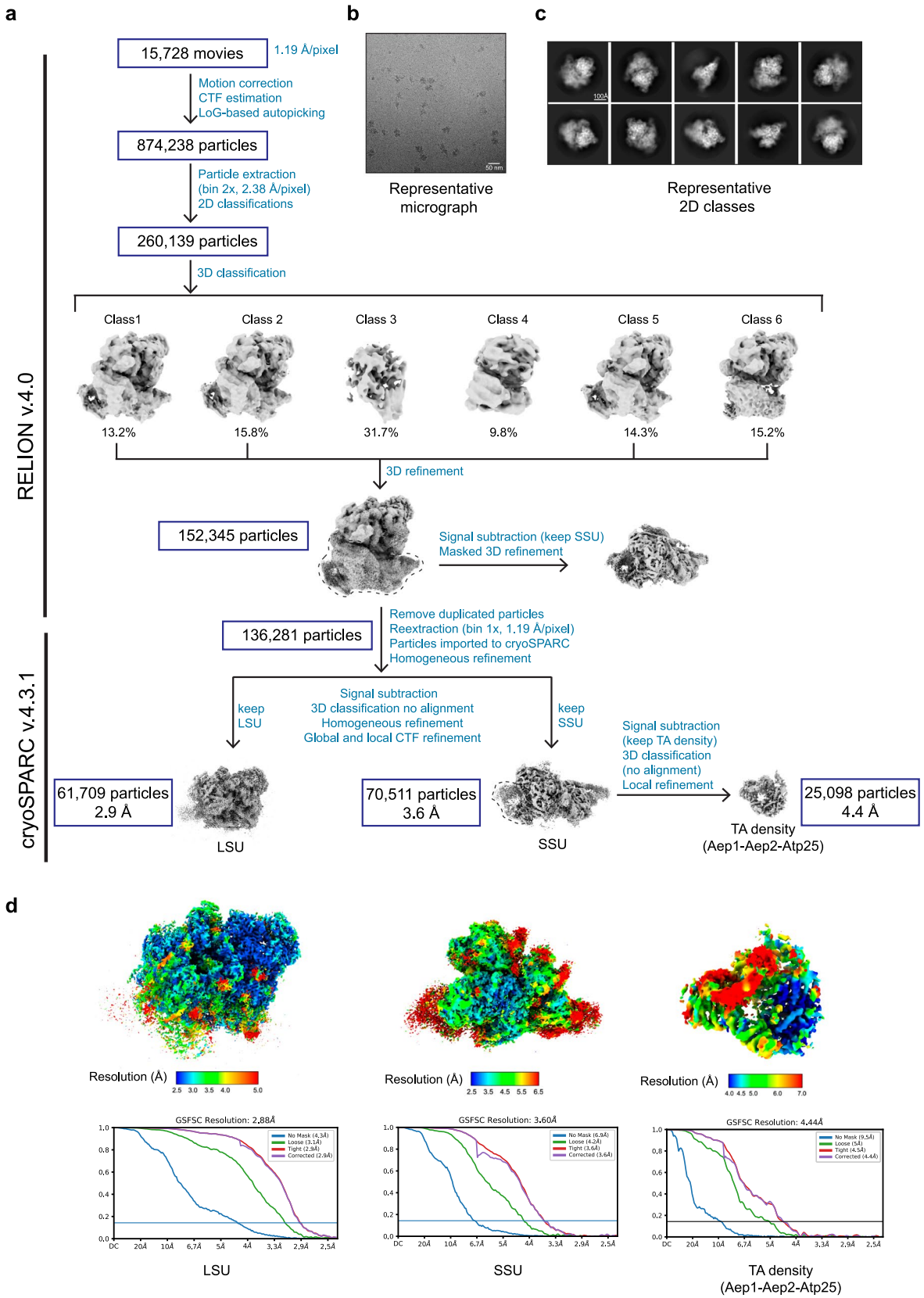

Extended Data Fig. 9 | Cryo-EM data processing for direct purification of Aep2-bound mitoribosomes. a, Flow chart showing details of cryo-EM data processing of Aep2-bound mitoribosomes in RELION v4.0 and cryoSPARC v.4.3.1, respectively. **b**, A representative micrograph is shown with scale bar corresponding to 50 nm. This experiment was repeated twice with similar results. **c**, Representative 2D classes of the Aep2-affinity purified mitoribosomes. **d**, Local resolution estimation (color coded to depict the local resolution of different parts) and gold-standard Fourier shell correlation (GSFSC) plot for each focused-refined map (FSC cut-off 0.143).

https://doi.org/10.1038/s41594-025-01726-y

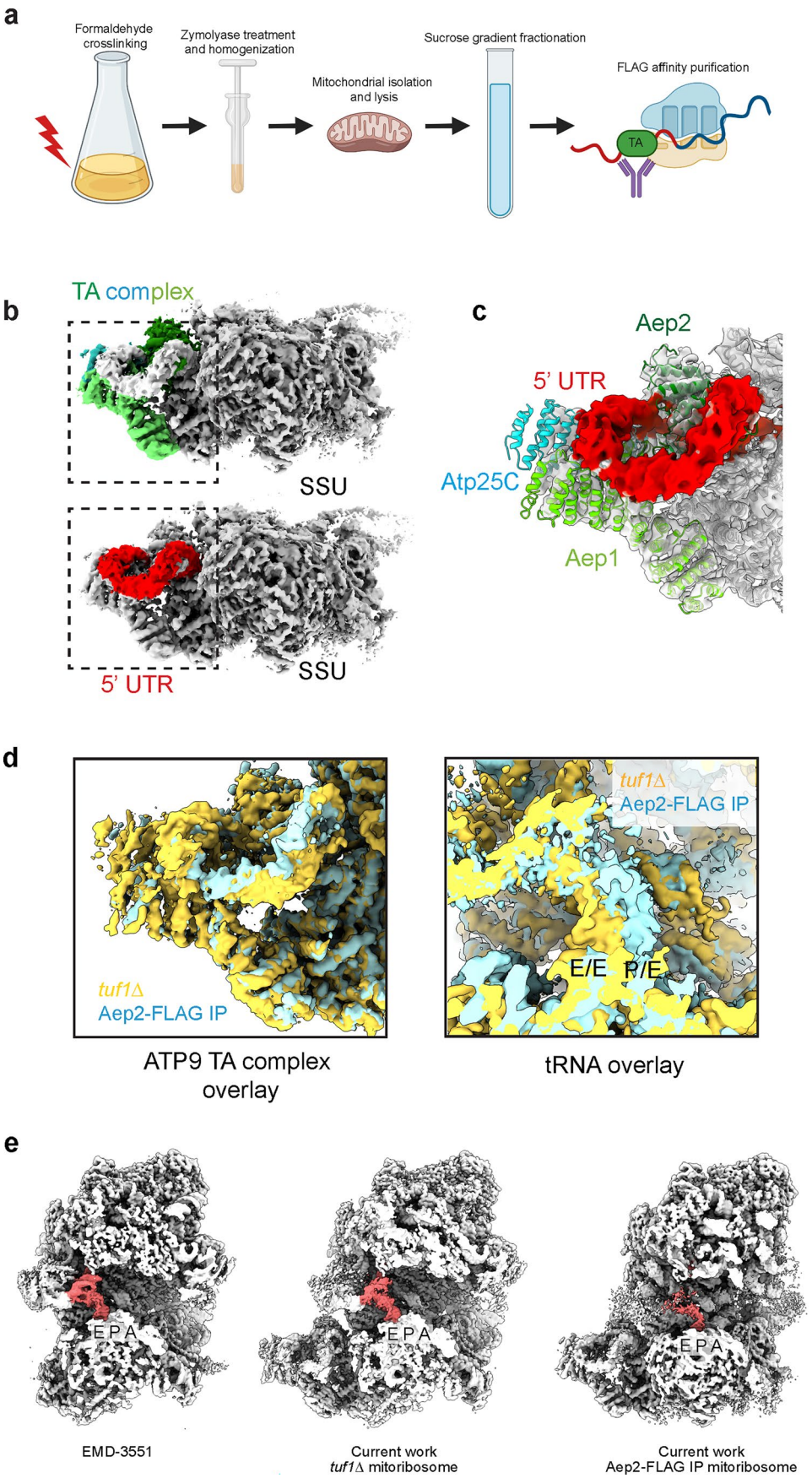

Extended Data Fig. 10 | See next page for caption.

https://doi.org/10.1038/s41594-025-01726-y

Extended Data Fig. 10 | Comparison between ATP9 TA bound mitoribosomes obtained from Aep2 affinity purification and *tuf1Δ* yeast cells. a, Illustration representing different steps for the sample preparation of the affinity purified Aep2-bound mitoribosomes. **b**, Composite map of the SSU, obtained from the Aep2-affinity purified mitoribosomes, bound to *ATP9* TA complex highlighting the color coded Aep1-Aep2-Atp25C density (left top) and 5'UTR density in red (left bottom). **c**, The structure of the *ATP9* TA complex from Fig. 3 fitted into the density of the Aep2-affinity purified mitoribosomes. **d**, Overlay of the cryo-EM densities of *ATP9* TA complex (left) and tRNA (right) obtained from the Aep2-affinity purified mitoribosome and *ATP9* TA complex bound mitoribosome obtained from *tuf1Δ* yeast cells. The affinity purified mitoribosomes are colored blue and the *tuf1Δ* mitoribosomes are colored yellow. **e**, Comparison of the tRNA position between previously published mitoribosome cryo-EM density map in the left panel (EMD-3551, low pass filtered) and ATP9 TA bound mitoribosome cryo-EM density maps obtained in this study (middle panel – obtained from *tuf1Δ* yeast cells, right panel - obtained from Aep2-FLAG affinity purification). Panel **a** created with BioRender.com.

nature portfolio

Corresponding author(s): L. Stirling Churchman, Martin Ott, and Sichen Shao

Last updated by author(s): Oct 24, 2025

Reporting Summary

Nature Portfolio wishes to improve the reproducibility of the work that we publish. This form provides structure for consistency and transparency in reporting. For further information on Nature Portfolio policies, see our Editorial Policies and the Editorial Policy Checklist.

Statistics

For all statistical analyses, confirm that the following items are present in the figure legend, table legend, main text, or Methods section.

n/a	Confirmed	
☐	☒	The exact sample size (*n*) for each experimental group/condition, given as a discrete number and unit of measurement
☐	☒	A statement on whether measurements were taken from distinct samples or whether the same sample was measured repeatedly
☐	☒	The statistical test(s) used AND whether they are one- or two-sided *Only common tests should be described solely by name; describe more complex techniques in the Methods section.*
☒	☐	A description of all covariates tested
☒	☐	A description of any assumptions or corrections, such as tests of normality and adjustment for multiple comparisons
☐	☒	A full description of the statistical parameters including central tendency (e.g. means) or other basic estimates (e.g. regression coefficient) AND variation (e.g. standard deviation) or associated estimates of uncertainty (e.g. confidence intervals)
☒	☐	For null hypothesis testing, the test statistic (e.g. *F*, *t*, *r*) with confidence intervals, effect sizes, degrees of freedom and *P* value noted *Give P values as exact values whenever suitable.*
☒	☐	For Bayesian analysis, information on the choice of priors and Markov chain Monte Carlo settings
☒	☐	For hierarchical and complex designs, identification of the appropriate level for tests and full reporting of outcomes
☒	☐	Estimates of effect sizes (e.g. Cohen's *d*, Pearson's *r*), indicating how they were calculated

Our web collection on statistics for biologists contains articles on many of the points above.

Software and code

Policy information about availability of computer code

Data collection	Sel-mitoRP reads were filtered and aligned to the sacCer 3 genome, which is described in detail in the Methods section. Cryo-EM data was collected using EPU (Thermo Fisher Scientific)
Data analysis	Cryo-EM image processing and analysis was performed using cryoSPARC (v4.3.1), RELION (v.4.0.1), CTF Find (v4.1), AlphaFold2/3, ChimeraX (v1.6), PHENIX (v1.21-5207), and Coot (v0.9.8.1). Sel-mitoRP data was processed using samtools (v1.9), bedtools (v2.27.1), cutadapt (v1.14), bowtie (v1.2.1.1), bamtools (v2.4.1), fastqc (v0.11.3), fastx (v0.0.13), igvtools (v2.3.88), star (v2.7.3a), and picard (v2.8.0). Custom scripts used to analyze and visualized the sel-mitoRP data are available at https://github.com/churchmanlab/Yeast_selective_mitoRP.

For manuscripts utilizing custom algorithms or software that are central to the research but not yet described in published literature, software must be made available to editors and reviewers. We strongly encourage code deposition in a community repository (e.g. GitHub). See the Nature Portfolio guidelines for submitting code & software for further information.

Data

Policy information about availability of data

All manuscripts must include a data availability statement. This statement should provide the following information, where applicable:

- Accession codes, unique identifiers, or web links for publicly available datasets
- A description of any restrictions on data availability
- For clinical datasets or third party data, please ensure that the statement adheres to our policy

Raw and processed sequencing data generated in this study were deposited in the GEO database under the accession number GSE282943. Mitoribosome footprints without crosslinking (steady-state glycerol growth) are available under accession number GSE74454.
Cryo-EM densities have been deposited at the Electron Microscopy Data Bank (EMDB) under accession codes EMD-52281 (Aep1-Aep2-Atp25C, composite), EMD-52235 (Aep1-Aep2-Atp25C, consensus), EMD-52270 (Aep1-Aep2-Atp25C, TA), EMD-52252, (Aep1-Aep2-Atp25C, SSU body), EMD-52256 (Aep1-Aep2-Atp25C, SSU head), EMD-52257 (Aep1-Aep2-Atp25C, LSU), EMD-52283 (Aep3, composite), EMD-52277 (Aep3, consensus), EMD-52276 (Aep3, TA), EMD-52278 (Aep3, SSU body), EMD-52279 (Aep3, SSU head), EMD-52280 (Aep3, LSU), EMD-48387 (Aep2-FLAG affinity purified, TA), EMD-48388 (Aep2-FLAG affinity purified, SSU), EMD-48390 (Aep2-FLAG affinity purified, LSU), and EMD-48700 (Aep2-FLAG affinity purified, composite map of SSU and Aep1-Aep2-Atp25C complex). Atomic models were deposited at the Protein Data Bank (PDB) under accession codes PDB 9HLZ (Aep1-Aep2-Atp25C, composite) and PDB 9HM0 (Aep3, composite). Other models utilized in this study are PDB 5MRC (yeast mitoribosome) and PDB 8OM4 (yeast mitoribosome, SSU).

Research involving human participants, their data, or biological material

Policy information about studies with human participants or human data. See also policy information about sex, gender (identity/presentation), and sexual orientation and race, ethnicity and racism.

Reporting on sex and gender	This is not relevant to the present study; human participants, their data, or biological material were not used.
Reporting on race, ethnicity, or other socially relevant groupings	This is not relevant to the present study; human participants, their data, or biological material were not used.
Population characteristics	This is not relevant to the present study; human participants, their data, or biological material were not used.
Recruitment	This is not relevant to the present study; human participants, their data, or biological material were not used.
Ethics oversight	This is not relevant to the present study; human participants, their data, or biological material were not used.

Note that full information on the approval of the study protocol must also be provided in the manuscript.

Field-specific reporting

Please select the one below that is the best fit for your research. If you are not sure, read the appropriate sections before making your selection.

☒ Life sciences ☐ Behavioural & social sciences ☐ Ecological, evolutionary & environmental sciences

For a reference copy of the document with all sections, see nature.com/documents/nr-reporting-summary-flat.pdf

Life sciences study design

All studies must disclose on these points even when the disclosure is negative.

Sample size	Sample sizes were not predetermined. At least two biological replicates were obtained for each western blot and sequencing experiment in line with other studies in this field and the data were found to be highly reproducible.
Data exclusions	No data were excluded from the study. Criteria for filtering of reads are included in the Methods section.
Replication	All experiments were performed in at least two biological replicates as is common in this field. All results were found to be highly similar and reproducible across replicates.
Randomization	Randomization is not relevant to our study. All experiments were carried out in yeast cell lines and sel-mitoRP for translational activators was compared to a control strain where the total mitoribosome population was isolated and footprints sequenced.
Blinding	Blinding was not relevant to our study. All sequencing and structure data was analyzed using unbiased computational approaches and software.

Reporting for specific materials, systems and methods

We require information from authors about some types of materials, experimental systems and methods used in many studies. Here, indicate whether each material, system or method listed is relevant to your study. If you are not sure if a list item applies to your research, read the appropriate section before selecting a response.

Materials & experimental systems

n/a	Involved in the study
☐	☒ Antibodies
☒	☐ Eukaryotic cell lines
☒	☐ Palaeontology and archaeology
☒	☐ Animals and other organisms
☒	☐ Clinical data
☒	☐ Dual use research of concern
☒	☐ Plants

Methods

n/a	Involved in the study
☒	☐ ChIP-seq
☒	☐ Flow cytometry
☒	☐ MRI-based neuroimaging

Antibodies

Antibodies used

Anti-FLAG (Millipore-Sigma, F1804, 1:1000), Anti-HA (Invitrogen, 26183, 1:1000), Anti-Myc (Millipore-Sigma, 05-724, 1:500), Anti-Mrp20 (Gruschke et al, 2010; PMID: 20404317), Anti-Mrpl4 (Gruschke et al, 2010; PMID: 20404317), Anti-Mrpl36 (Prestele et al, 2009; PMID: 19339279), Anti-Cox2 (Neupert lab, Munich, Germany), Anti-Tom70 (Rapaport lab, Tübingen, Germany), Anti-Tuf1 (This study), Anti-ALFA (NanoTag Biotechnologies GmbH, Göttingen, Germany. ID:N1580). Secondary antibodies used include IRDye 800CW goat anti-mouse secondary (LICORbio, 925-32210, 1:5000) and goat anti-rabbit IgG H L-HRP conjugate (BioRad, 1706515).

Validation

All commercially available antibodies have been validated by the manufacturer with validation data available on the respective manufacturer website. Anti-Mrp20 and Anti-Mrpl4 were previously published in Gruschke et al, 2010; PMID: 20404317 and were validated using deletion mutants. Anti-Mrpl36 was published in Prestele et al, 2009; PMID: 19339279 and was validated with deletion mutants. Anti-Cox2 was provided by the Neupert lab in Munich Germany and was validated using deletion mutants. Anti-Tom70 was a gift from the Rapaport lab in Tübingen, Germany and was validated using deletion mutants. Anti-Tuf1 was generated for this study and was obtained by immunizing rabbits with purified mature Tuf1. The anti-Tuf1 antibody was validated with deletion mutants of Tuf1 as can be seen in Extended Data Figure 5b.

Plants

Seed stocks

Report on the source of all seed stocks or other plant material used. If applicable, state the seed stock centre and catalogue number. If plant specimens were collected from the field, describe the collection location, date and sampling procedures.

Novel plant genotypes

Describe the methods by which all novel plant genotypes were produced. This includes those generated by transgenic approaches, gene editing, chemical/radiation-based mutagenesis and hybridization. For transgenic lines, describe the transformation method, the number of independent lines analyzed and the generation upon which experiments were performed. For gene-edited lines, describe the editor used, the endogenous sequence targeted for editing, the targeting guide RNA sequence (if applicable) and how the editor was applied.

Authentication

Describe any authentication procedures for each seed stock used or novel genotype generated. Describe any experiments used to assess the effect of a mutation and, where applicable, how potential secondary effects (e.g. second site T-DNA insertions, mosiacism, off-target gene editing) were examined.